

VQM3DA: A velocity and quality factor model of whole-mantle heterogeneity with anisotropy

Authors: Jesse F. Lawrence^{1,2*}, Michael E. Wysession¹

¹*Washington University in St. Louis, St. Louis, Missouri*

²*IGPP, Scripps Institute of Oceanography, La Jolla, California*

Submitted: Geochemistry, Geophysics, Geosystems, December, 2005

*Correspondence: jlawrence@ucsd.edu

Abstract

We present a 3-D tomographic model of shear velocity (V_S) and quality factor (Q_μ) for the whole mantle, VQM3DA, inverted from equivalent differential travel-time and attenuation data sets. By comparing similarly resolved V_S and Q_μ models it is possible to provide additional constraints on the geodynamic cause of many of the observed seismic anomalies. This study identifies and characterizes a variety of seismic anomalies in the mantle. In the upper mantle the highest attenuation is observed near subduction, presumably related to back arc spreading and dehydration melting. Vertical profiles across subduction zones exhibit some high Q_μ and high V_S slabs extending from the surface to the CMB. The African and Pacific superplumes possess low Q_μ and V_S . Long-wavelength correlation between V_S and Q_μ indicates significant thermal variation in the mantle. However, not all of the observed variations may be explained by temperature anomalies, and water content may play an important role. Vertical transverse anisotropy estimates for V_S and Q_μ are obtained from separate tangential and radial inversions. While the resolution of anisotropy is relatively poor, it is clear that anisotropy is stronger beneath subduction zones.

Introduction

Over the last several decades seismic tomography has increasingly gained finer resolution and greater reproducibility for the mantle [*Masters et al.*, 1982; *Dziewonski*, 1984; *Masters et al.*, 1996; *van der Hilst et al.*, 1997; *Grand et al.*, 1997; *Li and Romanowicz*, 1996; *Megnin and Romanowicz*, 2000; *Grand*, 2002; *Montelli et al.*, 2004]. However, our understanding of the causes of these anomalies has remained relatively unresolved by simply increasing resolution. It is very difficult to reliably differentiate between chemical, thermal, and phase change anomalies without comparing different types of tomographic results. For example, *Masters et al.* [2000] compared anomalous bulk sound velocity relative to compressional and shear velocities in the lowermost mantle beneath the Pacific to demonstrate the presence of chemical heterogeneity.

In general, correlation between *P*- and *S*-velocity anomalies indicates thermal anomalies, whereas the lack of correlation would suggest chemical heterogeneity [e.g., *Su and Dziewonski*, 1997; *Kennett et al.*, 1998]. Throughout most of the mantle there is good agreement between *P* and *S* velocities for multiple models [*Becker and Boschi*, 2002]. Several computational experiments of convective flow have been used to reproduce whole-mantle seismic tomographic models (e.g. *Ricard et al.*, [1993]; *Lithgow-Bertelloni and Richards*, [1995,1998]; *Bunge et al.*, [1998]; *Steinberger*, [2000]). Yet several disputes remain unsettled by simply improving the resolution of 3-D heterogeneous isotropic *P* and *S* velocity. For example, continued debate persists regarding the depths to which subducting slabs penetrate into the lower mantle [*van der Hilst*, 1997; *Puster and Jordan*, 1997].

Anisotropic tomography trails behind isotropic models in resolution. However, recent velocity inversions have solved for increasingly high-resolution anisotropy of the upper mantle [e.g., *Ekstrom and Dziewonski, 1998; Gung et al., 2003*]. Seismic anisotropy is indicative of high stress or layering in the mantle, suggesting different geodynamic origins. Anisotropy in the upper mantle is best constrained by surface waves, though body waves have some sensitivity to anisotropy in the lowermost upper mantle [*Wooky and Kendall, 2005*]. Recent anisotropy analysis has shown that continents possess anisotropic keels as deep as 400 km [*Gung et al., 2003*]. In the lower mantle, little-to-no anisotropy is measured either because of reduced sensitivity and data coverage or the lack of anisotropy. At the core-mantle boundary many types of anisotropy have been measured on many different length scales [*Kendall and Shearer, 1998a,b; Garnero et al., 2004; Panning et al., 2004*]. Further experimentation in whole-mantle anisotropy is important for demonstrating reproducibility and systematic relations between anisotropy and other types of tomography.

Further understanding has been gained by relating attenuation to seismic velocity [e.g., *Romanowicz, 1995; Roth et al., 1999; Fisher et al., 2003; Venkataraman et al., 2004*]. In the past decade there have been great improvements in global Q tomography of upper mantle structure [*Romanowicz, 1995; Selby and Woodhouse, 2000; Billien et al., 2000; Warren and Shearer, 2000; Gung and Romanowicz, 2004*]. Initially, most global Q studies involved the inversion of free oscillations and surface wave data. Global studies first resolved the depth dependence of Q by inverting for a globally-averaged radial model [e.g., *Dziewonski and Anderson, 1981; Widmer et al., 1991; Durek and Ekstrom, 1996*]. These models demonstrated that Q increases with depth, from low Q in

the asthenosphere ($Q_{\mu} \sim 80$) to high Q in the lower mantle ($Q_{\mu} \sim 350$). 3-D variations from these radial models have been calculated for the upper mantle with increasing accuracy and reproducibility [e.g., *Romanowicz, 1995; Selby and Woodhouse, 2000; Warren and Shearer, 2002; Gung and Romanowicz, 2004*]. However, complementary results for the lower mantle were lacking prior to this study.

Body wave attenuation measurements were improved through stacking and the advent of differential attenuation measurements [e.g., *Sipkin and Jordan, 1979, 1980; Flanagan and Wiens, 1990; Flanagan and Wiens, 1994; Roth and Wiens, 2001*]. Differential attenuation analyses of SS and S [*Bhattacharya et al., 1996*] demonstrated that global variations in shear attenuation were similar to those observed through surface wave data. Through stacking P - and PP -wave data, *Warren and Shearer [2002]* were able to quantify body wave attenuation for similar 3D varying structures for the upper mantle. *Fisher et al. [2003]* isolated small-scale lower mantle structures that exhibit correlated differential ScS - S attenuation and travel-time anomalies. *Lawrence and Wysession [2005a]* used globally averaged ScS - S data to construct a 1-D Q model (QLM9) that better satisfies the lower mantle contribution to differential attenuation. The large degree of variability in attenuation for all of these body wave studies indicates a large amount of 3-D heterogeneity throughout the mantle, including the lower mantle.

This study aims to constrain the 3-D Q_{μ} and anisotropy for the whole mantle for direct comparison with 3-D heterogeneous isotropic velocity anomalies. This study addresses several questions:

1. Are global Q_{μ} variations continuous between the upper and lower mantle?

2. If Q_μ anomalies do exist in the lower mantle, do they correlate with seismic velocity anomalies?
3. Is Q_μ anisotropic in either the upper or lower mantle?
4. If Q_μ is anisotropic, does the attenuation anisotropy correlate with velocity anisotropy, isotropic velocity, or isotropic Q_μ ?
5. What do the Q_μ , anisotropy, and velocity models tell us about the composition, temperature, phase change, and dynamic variations in the Earth?

In order to address these objectives we invert tangential and radial differential travel-times and attenuation measurements from multiple types of phase pairs for models of V_S and Q_μ , and SH/SV anisotropy using the same spatial resolution.

Data

Our data set consists of body wave data from which both attenuation and travel-time measurements are obtainable to ensure equivalence between attenuation and velocity inversions. While this requirement limits the data set, it increases our ability to directly compare the resultant models. Due to the higher sensitivity to noise and contamination, attenuation is the predominant limiting factor in quality control. In order to increase the accuracy of the attenuation measurement we use differential measurements between two seismic waves (e.g., the *ScS-S* [Fisher et al., 2003] or *SS-S* [Bhattacharya et al., 1996] phases).

We use two classes of differential measurements. The first involves two different seismic phases (e.g. *SS-S*) from the same seismogram [Jordan and Sipkin, 1977; Helmberger, 1983; Flanagan and Wiens, 1990], while the second consists of seismic ray

paths to many seismic stations for the same seismic phase from the same event [VanDecar and Crosson, 1990, Venkataraman et al., 2004]. Due to the increased difference in ray path geometries, the second method is more sensitive to noise, 3D heterogeneity, event mislocation, and source mechanism uncertainty.

In the first method, only phase pairs with normalized cross-correlation values and signal-to-noise ratios greater than 0.8 and 1.5 respectively are accepted. The differential travel-time and attenuation measurements are determined by cross correlation and the slope of the amplitude spectrum. We require that the waveform cross-correlation coefficient increases after attenuating the appropriate wave by the differential attenuation operator. In cases with negligible differential attenuation, this last requirement is waived. This requirement ensures that the attenuation is responsible for some of the waveform dissimilarity. Cross-correlation travel times are then recalculated after convolving the attenuation operator to determine the attenuation-corrected travel times.

The second class of differential measurement (multiple S phases at different stations) is more difficult to measure reliably. Therefore, more complex techniques are necessary. We employ the fast and efficient method of VanDecar and Crosson [1990], which uses the differential measurement between records from all station pairs for one earthquake to linearly solve for the relative attenuation at each station. The process is more stable because it relies on multiple differential measurements for each station rather than just one. However, coherence between signals decreases with increased distance between stations, increased frequency, and increased signal to noise. Therefore, we restrict the measurement to high root-mean-squared signal-to-noise ratios ($S:N > 3$), and weight the inversion according to the cross-correlation coefficient. Additionally, we only

apply this method to direct S waves, in order to avoid possible interference with other later shear waves. Because the mean differential S -wave anomaly relative to PREM is zero, the differential S -wave anomalies may be converted to absolute measurements.

Because other effects such as frequency-dependent diffraction around the core are dominant controls on amplitude spectra for diffracted waves like S_{diff} , we cannot use them in this study. This greatly reduces the resolution at the core mantle boundary. For this study we limit wave pairs to those directly relatable to the direct S -waves with epicentral distances between 45° and 85° . This distance range decreases the difference between S , ScS , SKS , and SS takeoff angles, which helps reduce differences between source functions and near-source structural anomalies. Encouraged by the success of this examination, future investigations will expand the distance range and number of phase pairs to include phases such as $SKKS$ - SKS and $ScS2$ - ScS .

We examined over 600,000 radial and tangential time series recorded at temporary and permanent broadband seismic station between 1990 and 2001. We used an event magnitude cutoff of $m_b > 5.7$. In addition to previously mentioned selection criteria, this study required visual confirmation of both the S and ScS phases, as these are the most important for isolating deep mantle structure. Other phases are less reliable indicators of signal quality (for example, SKS is usually not observable until beyond 60°). As a result, a total of only $\sim 35,000$ pairs of radial and tangential seismogram records met the criteria for inclusion in this study. The number of usable results is additionally limited by the requirement that each phase arrive more than 12.5 seconds separate from all other phases, reducing the chance of contamination and mistaken phase picking. From the above records, approximately 95,000 and 85,000 combinations of differential

measurements were obtained for tangential and radial phases, respectively. Table 1 indicates the breakdown by phase pair.

Figure 1 shows the distribution of seismic stations and earthquakes used in this study. To prevent highly sampled regions of the irregularly sampled Earth from controlling the inversion, we inversely weight the inversion by the square root of the sampling density. In order to remove adverse effects of laterally varying crustal structure, we corrected the travel-times with travel-time perturbations calculated from tracing each ray through CRUST 2.0 [Bassin *et al.*, 2000]. The crustal corrections are important for the phases with underside reflections off of the surface, like SS and sS , but otherwise have little effect on differential travel times.

Method

We invert the differential travel-time and attenuation data sets described above for 3-D heterogeneous V_S and Q_μ using ray theory approximations. Differential travel-times, dT , and attenuation operators, dt^* , are calculated from the difference in integrands between two ray paths. While this formulation imperfectly assumes that energy focuses along the ray paths, rather than through volumes defined by Frechet kernels [Dahlen *et al.*, 2000; Spetzler *et al.*, 2002], previous studies have shown that this assumption is reasonable for long-wavelength global tomography [e.g., Masters *et al.*, 1996; Masters *et al.*, 2000]. The ray path assumption is less problematic for attenuation inversion because the sensitivity for attenuation Frechet kernels more closely focuses along the geometrical ray path (in the hollow of travel-time ‘banana donut’ kernel [Zhao, personal communication, 2004]).

We divide the Earth into 12 layers of ~300 km thickness. Each layer is divided into 5-degree equal-area blocks resulting in $N=19,848$ model parameters. There are far fewer parameters than data, so the inversion is over-parameterized. However, some regions are still poorly sampled. The observed differential travel time (dT) and attenuation (dt^*) may be modeled by

$$dT_i = \sum_{k=1}^N [\Delta t_{2ik} - \Delta t_{1ik}] \Delta s_k \quad (1)$$

$$dt^*_i = \sum_{k=1}^N [Q_{Rk}^{-1} (\Delta t_{2ik} - \Delta t_{1ik})] \Delta Q_k$$

where the i^{th} pair of rays through the k^{th} block have finite reference travel times Δt_{1ik} and Δt_{2ik} . The k^{th} block has slowness perturbations Δs_k and quality Factor perturbation ΔQ_k from the reference quality factor Q_{Rk} . Equation 1 is equivalent to the invertible matrix formulation $\mathbf{d}=\mathbf{G}\mathbf{m}$, where the data vector \mathbf{d} is dT or dt^* , the sensitivity kernel \mathbf{G} is inside the brackets, and the model parameter vector \mathbf{m} is given by Δs or ΔQ . Zero-value model perturbations indicate that the velocity or quality factor model is equivalent to the radial models (PREM for velocity and QLM9 for quality factor), so a value of -1 would give a velocity or Q of zero. In this formulation, the percentage change in velocity and quality factor are given by $d\ln V_k = -\Delta s_k/(1+\Delta s_k)$ and $d\ln Q_k = -\Delta Q_k/(1+\Delta Q_k)$. Each perturbation must be greater than -1.0 to avoid singularities and negative velocities and quality factors.

Global tomography in the form of an overparameterized inversion requires *a priori* constraints to stabilize the results. Otherwise, inversions can become spiky, with unrealistic extreme perturbations [e.g., Menke, 1984]. In order to maintain smoothness,

we employ a first-derivative vertical and horizontal smoothing constraint, $\lambda \mathbf{m} = \mathbf{0}$. Because the inversions are heavily overparameterized, they are less sensitive to the smoothing constraints than other inversions that are more data-poor.

We also implement an average-model constraint that requires the average parameter of each layer to have a zero-sum perturbation from the mean spherically symmetric radial models PREM and QLM9. Good solutions typically have little difference between the input and inverted spherically-averaged radial models. We therefore involve a constraint matrix, $\boldsymbol{\psi}$, to ensure convergence toward the mean radially-symmetric model: $\boldsymbol{\psi} \mathbf{m} = \mathbf{0}$. The constraint ψ_{ik} is unity when the k^{th} block is in the i^{th} layer, and zero for all blocks in all other layers.

We invert a combined matrix, \mathbf{A} , such that modeled data and *a priori* constraints are satisfied. We have three conditions (\mathbf{G} , λ , and $\boldsymbol{\psi}$) and three sets of solutions (\mathbf{d} , $\mathbf{0}$, $\mathbf{0}$), which enable us to invert for the appropriate parameters that define the system,

$$\mathbf{A} \mathbf{m} = \begin{bmatrix} \mathbf{G} \\ a\lambda \\ b\boldsymbol{\psi} \end{bmatrix} \mathbf{m} = \begin{bmatrix} \mathbf{d} \\ \mathbf{0} \\ \mathbf{0} \end{bmatrix}. \quad (2)$$

This system has two weighting scalars, a and b , that respectively control the weighting for the smoothing and convergence toward the radial model. We employ the LSQR conjugate gradient method, which approaches the solution iteratively [Paige and Saunders, 1982] as described by Nolet [1987] and implemented by Masters *et al.* [2000]. LSQR is especially efficient for large sparsely-sampled matrix inversions, such as the one inverted here. However, LSQR does not allow for true resolution tests, so we rely on

checkerboard tests instead. By tracing all of the rays used in our inversion through a theoretical Earth with a checkerboard pattern of fast and slow, or attenuating and non-attenuating anomalies, we determine whether the resolution is sufficient to resolve different-sized structures. Each ray trace accumulates an anomalous travel time or attenuation. If the inversion of these theoretical travel-time and attenuation values returns the correct checkerboard pattern, then we have resolution down to the scale of the checkerboard. While less informative than a linear resolution matrix [Boschi, 2003], the inverted checkerboard visually demonstrates how anomalies are dampened, smoothed, smeared, and distorted by the inversion process. We determine the correct pair of weighting scalars, a and b , by comparing input and inverted checkerboard patterns. The best scalar pair yields the greatest correlation between the input model and resultant model in the checkerboard test. Figure 2 shows the input and inverted checkerboard models of the best pair. Given the excellent agreement between large-scale features, we find that the resolution is sufficient to continue examining the global pattern of Q_μ and V_S .

3.3 Radial Anisotropy:

Tangential- and radial-component models may be used to estimate velocity and attenuation anisotropy. Travel times and attenuation measured on tangential-component records only depend on horizontal velocity, V_{SH} , and quality factor, Q_{SH} . Radial-component travel times and attenuation depend on horizontal velocity and quality factor and vertical velocity, V_{SV} , and quality factor, Q_{SV} . Given a known ray path with known incidence angle, i , it is possible to determine the horizontal and vertical contributions to

the radial component from the tangential and radial component velocities. Using the geometry shown in Figure 3 and assuming no azimuthal anisotropy, the radial-component slowness (s_R) is given by Equation 3

$$s_R = \frac{1}{V_R} = \left(\frac{\cos^2(i)}{V_{SH}^2} + \frac{\sin^2(i)}{V_{SV}^2} \right)^{1/2}. \quad (3)$$

The horizontal velocity is well defined by the tangential velocity as

$$V_{SH} = V_T. \quad (4)$$

The vertical velocity is therefore determined using

$$V_{SV} = \left(\frac{1}{\sin^2(i)V_R^2} - \frac{1}{\tan^2(i)V_T^2} \right)^{-1/2}. \quad (5)$$

We argue that Q_μ follows the same principles and may be solved in the same manner. Using the vertical and horizontal velocities and Q_μ calculated from Equations 4 and 5, we can solve for the isotropic velocity perturbation, $d\ln V_{ISO}$, and quality factor, $d\ln Q_{ISO}$, with respect to the reference model as

$$d\ln V_{ISO} = (d\ln V_{SV} + d\ln V_{SH})/2. \quad (6)$$

The above assumptions ignore alternate forms of anisotropy such as azimuthal and dipping transverse anisotropy. Consequently, if alternate forms of anisotropy affect the radial and tangential component, then these alternate form of anisotropy may be misinterpreted as radial anisotropy. Sufficient azimuthal coverage would remove effects of azimuthal and dipping transverse anisotropy by way of averaging the different azimuthal contributions. However, the inevitably uneven azimuthal sampling maps some azimuthal anisotropy into radial anisotropy. This needs to be kept in mind when interpreting the results.

A decrease in sensitivity to upper mantle anisotropy is another beneficial consequence of using the prescribed differential geometries and assumptions. The ray paths of differential phases are similar at shallow depths, so anisotropy effects both phases in a similar manner. Therefore, the differential analysis de-emphasizes contaminating effects of azimuthal anisotropy in the upper mantle, where it is greatest. However, this is compromised to some degree by the fact that close to the surface, using Equation 5, the V_{SV} and Q_{SV} calculations rely more on the transverse component, which is in a direction that is perpendicular to the horizontal component in the radial direction, and therefore increases the susceptibility to contamination from azimuthal anisotropy.

The tangential and radial data sets are not identical, which leads to differences in lateral coverage within our tangential- and radial-component models. These differences can contaminate the evaluated anisotropy signature. For these reasons we conduct a series of checkerboard tests to determine if there is sufficient resolution to justify examination of anisotropy for both velocity and attenuation. Long-wavelength resolution is recovered for checkerboards with lateral dimensions greater than 40° , but for blocks

smaller than about 36° the resolution becomes spotty. The 36° checkerboard can be used to show where resolution is high and low (Figure 4). Within confined regions there is sufficient agreement between the input and inverted anisotropic checkerboard results for examination of shorter-wavelength anomalies. The highest resolution occurs below subduction zones in the lower mantle. As expected, upper mantle anisotropy anomalies are poorly resolved due to the small amount of vertical particle motion.

Results

Depth Sections:

Figure 5 shows lateral cross-sections through our isotropic velocity model at depths from the surface to the core-mantle boundary. Fast-velocity anomalies may be found underlying subduction zones and continents in the shallow layers. Seismically slow anomalies are found in shallow regions underlying oceanic crust and mountain building regions. The lack of surface wave data in this study significantly reduces the resolution of upper mantle anomalies. This is especially true for regions with poor SS-wave coverage. Nevertheless, the gross upper mantle structure agrees with the models of *Megnin and Romanowicz* [2000], and *Masters et al.*, [1996, 2000].

The strongest anomalies observed in the lower mantle occur near the core-mantle boundary. The high-velocity signature of paleo-subduction persists throughout the entirety of the lower mantle beneath North America. The seismically fast anomaly associated with Farallon paleo-subduction progresses eastward with depth, which is in agreement with *Grand* [1994], *Grand et al.*, [1997], and *van der Hilst et al.*, [1997]. Subduction beneath the Kamchatka, Japan, and Mariana trenches likely continues into the lower mantle, where high-amplitude fast anomalies extend to depths in excess of

1500km. There is less indication of continued subduction into the lower mantle subduction beneath the Tonga-Kermadec, where resolution is much lower. Seismically fast anomalies associated with South American subduction have little continuity above ~1900 km. All of these observations are in agreement with typical global models such as *Megnin and Romanowicz* [2000] and *Grand* [2002]. The African and Pacific large-scale slow anomalies in the lower mantle have the strongest signal near the core-mantle boundary, decaying upward to a depth of about 1400 km.

The isotropic Q_μ model has lateral cross-sections (Figure 6) that are in some places similar, but in others distinctly different from our isotropic velocity cross-sections. In the upper mantle, the highest Q_{ISO} anomalies are observed underlying the continent side of continent-ocean subduction zones. The lowest Q_{ISO} anomalies occur beneath the ocean side of subduction zones in shallow layers. Mantle beneath the oceans is more attenuating than beneath the continents. This largely agrees with other attenuation models [*Romanowicz*, 1995; *Warren and Shearer*, 2002; *Gung and Romanowicz*, 2003; *Reid et al.*, 2001]. The observable differences between the various upper mantle quality factor models are likely the result of resolution differences and the differences between surface wave, P -wave, and S -wave sensitivities in inversions.

Underlying North America and Asia, at a depth of ~670 km, there is a significant change from the predominant upper mantle high- Q_μ anomalies to lower mantle low- Q_μ anomalies. This reversal continues from the 670 km discontinuity to about 1400 km. At greater depths, the structure becomes more similar to that of the upper mantle, with high- Q_μ anomalies underlying continents near subduction zones. Underlying the Pacific Rim, small cores of high Q_μ persist from the 660 km discontinuity to approximately 1300 km.

With increasing depth, the high- Q_μ anomalies around the Pacific become more pronounced in both amplitude and lateral dimension. At the core-mantle boundary, high- Q_μ anomalies are larger and higher in magnitude than anywhere else in the mantle. Low Q_μ anomalies persist from crust to core beneath the East Pacific, Indian, and Atlantic Oceans. The amplitudes of these attenuation anomalies increase with depth.

Correlation between V_S and Q_μ models changes significantly with depth. The highest correlation between Q_μ and V_S anomalies for a whole layer occurs within the lowermost mantle ($R^2 = 0.4$) and uppermost mantle ($R^2 = 0.3$), which is still not very significant. The weakest correlations occur between depths of ~ 800 km and ~ 1300 km, where the Q_μ reversal beneath Asia and North America occurs. At a depth of ~ 1000 the correlation even becomes negative ($R = -0.2$),

Anisotropy:

As mentioned above, the resolution within the upper mantle is minimal. However, some discernable pattern is visible in the horizontal cross-sections through the anisotropic velocity model (Figure 7). In general, anomalously-fast V_{SH} is observed beneath continents and active margins. While we present these layers with some trepidation, and indicate that amplitudes are not well represented, the upper mantle pattern of anisotropy does agree with previous results from SAW16AN [Gung *et al.*, 2003]. Below 1200 km, sheet-like V_{SV} -fast structures are found beneath North America, Northern Asia, and South East Asia, where the model resolution is highest. Within the lower mantle, the largest-amplitude fast- V_{SH} regions are observed flanking these sheet-like structures. A lower-amplitude fast- V_{SV} structure broadens with depth over this same

depth range underlying the East Pacific rise. At the core-mantle boundary, broad high- V_{SH} regions are located adjacent to thinner high- V_{SV} sheet-like structures. Again, this lowermost mantle structure agrees with SAW16AN [Panning *et al.*, 2004].

Lateral cross-sections of upper mantle attenuation anisotropy (Figure 8) are marked by high Q_{SH} beneath Asia, with the largest magnitude anomalies occurring near the Pacific Rim. Due to reduced resolution at shallow depths, this is the only region where smaller-scale anisotropy is resolvable. From depths of ~ 1000 km to the core-mantle boundary, sheet-like high- Q_{SV} anomalies are observed around the Pacific Rim. Aside from a slightly high- Q_{SV} region beneath Africa, the remainder of the lower mantle is mildly high in Q_{SH} .

Vertical Sections:

Vertical profiles (Figure 9) of anomalous isotropic velocity, isotropic quality factor, velocity anisotropy, and anisotropic quality factor show a striking increase in anomaly magnitude near subduction zones. The largest isotropic high- V_S and high- Q_{ISO} anomalies occur beneath subduction zones at the surface and the CMB. At the top of the lower mantle, large magnitude low- Q_{ISO} anomalies are found in many places. Both Q_μ and velocity anisotropies show a high correlation with Q_{ISO} . Non-subduction zone regions have less-significant anomalies.

Vertical Q_{ISO} profiles parallel to the dip of subduction (Figure 10) show high- Q_{ISO} anomalies spanning from the surface to the CMB. The most clearly resolved of these anomalies are those below the edges of Asia and North America, where the highest resolution is obtained. The continental sides of most ocean-continent subduction zones

are marked by low- Q_{ISO} values between 670 km and ~1400 km. Vertical Q_{ISO} and V_S profiles through Africa and the Pacific Ocean (Figure 10) are marked by large low- Q_{ISO} and low- V_{ISO} anomalies extending upward from the CMB with decreasing amplitude. Underlying spreading ridges, the low- Q_{ISO} and low- V_{ISO} anomalies extend from the crust to the core-mantle boundary, where they are at their maxima. Away from spreading ridges, these large low- Q_{μ} anomalies are limited to the lower mantle.

Discussion

The three most notable features of VQM3DA are 1) the high- Q_{μ} and high- V_S anomalies spanning from crust to core around the Pacific rim, 2) low- Q_{μ} and low- V_S values from crust to core beneath spreading ridges and 3) the significant change in Q_{μ} structure from the 670 km discontinuity to ~1400 km underlying the down-dip side of ocean-continent subduction zones. This study clearly demonstrates that the pattern of transition zone Q_{μ} variation extends into the lower mantle, as postulated by *Gung and Romanowicz* [2002]. However, the style in which the seismic quality factor continues to deeper depths is unexpected and intriguing, which suggests complex interactions between possible variations in chemical composition, temperature, grain size, phase change, and stress.

Though the velocity model of VQM3DA has a lower resolution than many modern tomographic models, the tomographic images presented here do have common features that reproduce previously observed anomalies (where comparable data exists). Once we have addressed the reliability of our model, we can proceed to describe some methods by which to interpret the various anomalies. We will then discuss several

anomalies in the model and draw geophysical inferences regarding the imaged mantle features.

Reproducibility and model evaluation:

As mentioned in the methods section, the checkerboard (Figure 2) and spike tests resulted in sufficient model recovery to warrant long-wavelength evaluation of the isotropic V_S and Q_μ models. Resolution is highest beneath northern hemisphere continents, lowest in the central Pacific, and vertically smeared in the upper mantle. While the anisotropic models are less robust due to differences in radial and tangential data, the models are still capable of resolving long-wavelength structure. Nevertheless, the amplitudes of the anisotropic models are often over and underestimated due to the difference in vertical and horizontal sensitivities associated with dominant ray parameters.

The strong similarity between these results and those found in the literature (where available), suggests that despite large differences in data and methods, the long-wavelength structure is robust and reproducible. These similarities are highlighted in Figure 11. The agreement between QRLW8 [Gung and Romanowicz, 2004] and VQM3DA is excellent for depths between 300 km to 660 km despite the fact the models are constructed using very different theory, inversion methods, and data (Figure 11a). The convergence of different models using different data and techniques is one of the best indications of their successful resolvability. This happened in the 1990's with velocity tomography, and is only now happening with attenuation tomography. QRLW8 is a model constructed from a spherical harmonic degree-eight inversion of long-period

(60-400s) surface wave dispersion and overtones, whereas VQM3DA uses shorter-period (12-33s) body waves in a block-model inversion. QRLW8 loses resolution with depth, limiting the model to the upper mantle and transition zone, whereas VQM3DA vertically smears in the upper mantle, yielding poorer results for shallow (< 200 km) structure. The observation of significant model similarity for 300-600 shows that these Q_μ models are both robust at depths below 300 km. There are no models with which to compare lower mantle quality factor. The similarity between the long-period surface wave and shorter-period body wave models indicates that Q_μ is not strongly frequency dependent, which demonstrates that future experiments can use joint inversion of surface wave and body wave data to yield higher-resolution, more robust models.

Though lower in resolution, our long-wavelength isotropic velocity model agrees well with previous models such as SB4L18 [Masters *et al.*, 2000] for most regions (Figure 11b). For example, the Farallon slab appears to be deflected to the east into the upper portion of the lower mantle [e.g., Grand, 1994; Grand *et al.*, 1997; van der Hilst *et al.*, 1997]. However significant differences are observed as a result of differences in resolution and large differences in data. Our travel times are corrected for attenuation, whereas previous travel times used in inversions were not. Consequently, our technique reduces the anelastic delays to travel times caused by attenuation-related dispersion. This is a significant strength of our model.

The global pattern of anisotropic velocity is poorly resolved relative to isotropic velocity. Therefore, we only compare the long-wavelength (harmonic degree $l < 8$) pattern of anomalous anisotropic velocity with that of SAW16AN [Gung *et al.*, 2003; Panning *et al.*, 2003] in Figure 11c. In both models, the mean anisotropy of each layer is

removed to show relative variations [Figure 12]. In the upper mantle, fast- V_{SH} (red) anomalies are observed beneath the continents and down-dip of subduction zones. The East Pacific Rise also stands out as a relatively high- V_{SH} region. In the lower mantle, the pattern is less relatable to surface geometries. Nevertheless, the long-wavelength patterns appear similar. For example, the alternating pattern of anisotropy in the Pacific is quite visible [e.g., *Lay et al.*, 1998]. This similarity is reduced in the southern hemisphere, where fewer data were available.

There are no previous models with which to compare our anisotropic quality factor model, so we cannot comment on the reproducibility of this model. Instead, we rely on the strengths of the isotropic Q_{μ} model and anisotropic V_S models to indicate that the models are robust. Even with the lower resolution, our long-wavelength anisotropic velocity structure is remarkably similar to the radial anisotropy model, SAW16AN [*Gung et al.*, 2003; *Panning et al.*, 2004] at the upper and lower mantle boundaries.

Elastic v. Anelastic Effects on Attenuation:

One question to consider before interpreting the observed attenuation anomalies is whether the differential attenuation measurements adequately isolate anelastic structure. Amplitude variations can result from a variety of elastic sources such as small-scale scattering, waveform focusing, and directional source mechanics. Although we attempt to reduce the effects of elastic amplitude variation through our differential measurement techniques and data selection criteria, some elastic contamination may still persist. The differential measurement approach effectively removes the directivity effects of each seismic source [e.g., *Bhattacharya et al.*, 1996]. Only waves departing the source on

different sides of a nodal plane, or near the nodal plane have largely different source functions; two such waves would have a low correlation coefficient, and would not fit the data selection criteria.

Waveform focusing, defocusing, and multipathing can cause significant amplitude variations, which in turn may contaminate attenuation. Because of wavefront annealing the observed amplitude variation due to 3D heterogeneity is proportional to the amplitude of the velocity anomaly and inversely proportional to the distance between the encountered anomaly and the seismic receiver. Consequently, large-amplitude 3D velocity anomalies near the receiver have the largest effect on amplitude. While the uppermost mantle is the region most likely to cause spurious amplitude variations due to high-amplitudes velocity heterogeneity, the differential measurements largely reduce the effects of amplitude variation near the receiver because the phases have overlapping upper mantle sensitivities. It is also possible for 3D anomalies to result in multiple waves that arrive nearly simultaneously, resulting in significant waveform perturbation. Such a waveform would result in a low correlation coefficient between individual phases, which would result in exclusion from this study. Nevertheless, some cases of less severe waveform perturbations due to 3D structure might maintain high correlation and meet selection criteria.

As *Cormier* [2000] showed, scattering from small-scale heterogeneities can, in some cases, cause pulse broadening that has a similar appearance to the effects of anelasticity. Little is known about small-scale heterogeneity in the lower mantle. There is evidence of mantle scattering northeast of the Mariana subduction zone from *S*-to-*P* conversions, which *Kaneshima and Helffrich* [1998] interpreted as chemically-distinct

reservoirs. Small fragments of ancient subducted slabs may be responsible for seismic reflections observed at ~1600 km depth [Kaneshima and Helffrich, 1999; Castle and van der Hilst, 2003]. These fragments may be as small as ~8 km in diameter [Helffrich, 2002]. Even smaller heterogeneity (< km diameter) has been observed at the base of the mantle [Brana and Helffrich, 2004].

Although small and large 3D structure can change amplitudes and contaminate attenuation measurements, it is unlikely that 3D heterogeneity can cause amplitude variation that matches the effects of constant- Q for a wide frequency band (0.01 - 0.1 Hz). We apply the observed attenuation operator to each waveform pair and ensure that correlation increases as a result (or stays constant for null differential attenuation) before using the measurement in the study. Consequently, only measurements that fit the expectation of frequency independent- Q are used in the study.

The process of long-wavelength inversion effectively reduces the potential for 3D structure to contaminate the quality factor model. Focusing, defocusing, and multipathing are directionally dependent; so multiple paths through the same highly heterogeneous region would result in variable differential measurements. Given a highly overparameterized and damped inversion, the effects of 3D heterogeneity will largely average out. Advances in theoretical seismology need to be made in order to adequately measure the seismic attenuation of body phase resulting 3D heterogeneity in the mantle. However, the good agreement between the various body wave and surface wave attenuation/ Q studies for the upper mantle indicates that scattering is much less of an effect that previously feared.

Interpretation of Anomalies:

Velocities change as a result of anharmonic and anelastic variations, whereas the response of Q_μ , if not caused by elastic scattering and multipathing, is anelastic. Therefore, attenuation and velocity variations both have different dependencies upon grain size, temperature, composition, and stress. The patterns of V_S and Q_μ anomalies are indicative of the state of the stress, temperature, composition, and grain size, though, unfortunately, in non-unique ways. Laboratory experiments have begun to quantify the dependencies of V_S and Q_μ upon these factors [e.g., *Karato et al.*, 1993; *Jackson et al.*, 1992, 2002; *Getting et al.*, 1997]. *Karato* [2003] finds that water content and temperature are the largest components effecting attenuation at any given depth or pressure. Consequently, they may be related to temperature through

$$\log\left(\frac{Q^{-1}}{Q_0^{-1}}\right) \cong \alpha r \log\left(\frac{C_{OH}}{C_{OH_0}}\right) - \frac{\alpha H^*}{R} \left(\frac{1}{T} - \frac{1}{T_0}\right) \quad (7)$$

where α is the frequency dependence ($\alpha = 0.25 \pm 0.03$), r is 1.2 for ‘wet’ olivine, C_{OH} is the concentration of OH, H^* is the activation enthalpy ($H^* = 500 \pm 200$ kJ/mol), R is the gas constant, and T is temperature [*Karato*, 2003; *Jung and Karato*, 2002]. The zero subscript indicates a reference level of OH, T , and Q_μ from which anomalous values can be gauged. Therefore, anomalous Q_μ may be calculated as a result of water content and temperature. While insightful, the constants for the temperatures, pressures, and mineral assemblages appropriate for the lower mantle have not been fully explored, so the equations cannot be directly used to calculate true variations in lower mantle Q_μ .

Water has less effect on seismic velocity than attenuation [*Karato*, 2003] because dispersion is less effective at delaying waves than the anharmonic effects of thermal

expansion. The relationship between water, temperature and seismic velocity is described by *Karato* [2003] as

$$d\ln V(\%) \cong -A(P)\delta T - FQ_0^{-1} \left[\left(\frac{C_{OH}}{C_{OH_0}} \right)^{r\alpha} \exp\left(\frac{\alpha H^* \delta T}{RT_0} \right) - 1 \right] \quad (8)$$

where $A(P)$ is the pressure dependent anharmonic effect due to thermal expansion ($\sim 7 \times 10^{-5} \text{ K}^{-1}$), δT is the temperature anomaly, and F is the frequency dependence ($\cot(\pi\alpha/2)/2$) [*Minster and Anderson*, 1981]. Given $\alpha = 0.25$, attenuation has a fourth-root dependence on the dominant grain size [*Jackson, et al.*, 1992, 2002] giving rise to a $\sim 77\%$ variation in Q_μ as a result an order-of-magnitude increase in grain size.

We can describe perturbations in seismic velocity and quality factor as a result of water and temperature variations using Equations 7 and 8 (Figure 13) [*Karato*, 2003]. Note that the exact perturbations presented here are only appropriate for a particular set of conditions ($\alpha = 0.25$, $A \sim 7 \times 10^{-5} \text{ K}^{-1}$, $H^* = 500 \text{ kJ/mol}$) in the upper mantle, but Figure 13 demonstrates a general pattern of expected variation for typical compositions and pressures. The water content changes by an order of magnitude relative to a non-dimensional average, whereas the temperature varies from -25% to 50%. Clearly, attenuation varies much more than velocity. Because the velocity changes less with water content than temperature does, it is possible to distinguish between water and temperature anomalies when examining velocity and attenuation variations simultaneously.

Anisotropic velocity perturbations increase due to deviatoric strain when larger grains align, but can only accrue in a dislocation-creep environment [*McNamara et al.*, 2002]. If not, then diffusion creep breaks down the anisotropy. Generally, diffusion

creep dominates at high temperatures and low stresses, whereas dislocation creep occurs at low temperatures and high stresses. Consequently, lattice-preferred orientation (LPO) is only expected to accrue at low temperatures and high stresses where Q_μ and V_S should be high [e.g., *McNamara et al.*, 2003]. While no laboratory experiments have systematically analyzed the dependencies of anisotropic Q_μ , we surmise that alignment of crystals and deviatoric strain might result in anisotropic Q_μ . Again, the alignment of crystals in a cold, high-stress environment necessary for dislocation creep indicates that anisotropic variations in Q_μ should accumulate in high- Q_μ regions.

The dominant mechanisms for upper mantle attenuation are generally thought to be diffusion creep and dislocation creep [e.g., *Karato et al.*, 1996; *Gribb and Cooper*, 1998; *Cooper et al.*, 2002; *Karato*, 2003], but other forms of deformation cannot be ruled out for the lower mantle. Due to the general lack of anisotropy in the majority of the lower mantle, the lower mantle is assumed to be in a diffusion-creep-dominated environment [*Karato et al.*, 1995]. Water can effect both grain boundary and intra-granular processes, potentially decreasing quality factor and, to a lesser extent, velocity. In addition, water can increase grain boundary and intra-granular deformation, causing increased anisotropy [*Karato*, 1993].

Using the above assertions about quality factor, anisotropy, and velocity, it is possible to qualitatively describe some anomalies within the Earth. For example, the very high attenuation in the upper mantle beneath subduction zones could indicate either elevated temperature or elevated water content. Because we know that slabs are cold, only water can account for the observation of high attenuation in the upper mantle wedge. Water content likely increases with age in oceanic crust as a result of serpentinization

prior to subduction. After subduction, dehydration of the slabs likely increases grain boundary deformation at shallow depths (~100 km) [Iwamori and Chau, 2000]. Attenuation within the mantle wedge is extremely high due to this process [e.g., Flanagan and Wiens, 1994; Roth et al., 2000; Stachnik et al., 2004]. Seismic velocities are also very low in this region because the addition of water causes the material to approach and, in some regions, exceed its melting temperature.

The low- Q_μ anomaly found down-dip of western Pacific subduction between 660 and 1400 km depth may be interpreted as either extremely warm or highly water-saturated. The heat source necessary for a thermal anomaly of such large scale ($d\ln Q_\mu < -5\%$ yields a volume of 1.8×10^{10} km) would have to be enormous in order to create such a large low- Q_μ anomaly. In addition, we see less-pronounced low- V_S perturbations accompanying the large low- Q_μ anomaly, suggesting that the pattern is more similar to that of water. The anomaly is bound on the Pacific side and bottom by high- V_S and high- Q_μ paleosubducted slabs, so it is unlikely that the anomaly could penetrate through, nor circumnavigate the entirety of the cold slab. It is more likely that the dense hydrous mineral phase D dehydrates at 1100-1400 km depth within a cold downwelling slab, supplying water to otherwise anhydrous minerals [Li and Jeanloz, 1991; Sheih et al., 1998]. The effect would be similar to upper mantle dehydration within the mantle wedge [Sheih et al., 1998]. Because the lower mantle mineral assemblages have extremely low water solubility (< 0.2 wt% [Ohtani, 2005]), small amounts of dehydrated water can filter into the region overlying the slab, resulting in very large attenuation anomalies. Ringwoodite and wadsleyite can hold much higher water concentrations, so the slight increase in water in the transition zone in this location above the anomaly would produce

little-to-no seismic signal in V_S and Q_μ . A lower mantle dehydration model would explain why the anomaly is observed down-dip of subduction in the 600-1500km depth range with such strength.

The remainder of the mantle appears largely homogeneous in comparison to the large amplitude anomalies observed near subduction zones. In general, the shallow mantle beneath continents is both seismically fast and low-attenuating, requiring low temperatures and water content. The elevated Q_μ and V_S found beneath the continents dissipates with depth by ~660 km, though vertical smearing limits our ability to judge the actual bottoming depth. In the lower mantle, the largest anomalies not related to subduction are broad low- V_S and low- Q_μ anomalies rising up from the CMB beneath Africa and the Pacific. There is no known mechanism capable of transporting water to the base of the mantle, so these anomalies likely result from thermal or chemical variations. There is much discussion as to whether these megaplumes beneath Africa and the Pacific are chemically distinct from the surrounding mantle [Wen *et al.*, 2001; Wen, 2002]. However, whether or not it is chemically distinct, its proximity to the core-mantle thermal boundary layer would make it anomalously hot, causing a decrease in both Q_μ and V_S , and resulting in a higher correlation between the two.

While there are many similarities between the V_S and Q_μ anomalies, there are also some interesting differences between them. For example, the Farallon slab (Figure 10) is concave when imaged by velocity, which agrees with [Grand, 1994; Grand *et al.*, 1997; van der Hilst *et al.*, 1997], but convex when imaged with Q_μ . There is a large, low- V_S and low- Q_μ anomaly that spatially separates the two. Neither the Q_μ slab nor the V_S slab is an artifact of the inversion process, as both are easily resolvable features. In fact, there

appears to be a second, lower-amplitude high- V_S slab collocated with the high- Q_μ slab that extends through the upper lower mantle beneath the western edge of North America. This feature has been observed in previous tomographic velocity models [*Masters et al.*, 2000; *Grand*, 2002]. At the present, it is not clear which combination of factors (temperature, grain size, composition, or stress) are responsible for this difference, or if small-scale scattering or waveform multipathing could make the Farallon appear higher attenuating than other subducted lithosphere.

Subduction

Around the edge of the Pacific, subduction zones coincide with sub-vertical high- Q_μ and high- V_S anomalies spanning from the crust to the core. In the northern hemisphere, where resolution of our model is best, these high- Q_μ anomalies are primarily sheet-like structures, following the pattern of subduction. The Q_μ anomalies related to subduction zones range in lateral thickness from less than 1000 km within the mid and upper mantle to more than 4000 km at the CMB. The magnitudes of the Q_μ anomalies also increase with depth from ~5% up to ~60%. We interpret the widths and magnitudes as upper and lower limits, respectively, because smoothing and the large inversion block-size tend to broaden and dampen the anomalies.

As previously mentioned, velocity anisotropy and attenuation anisotropy are both elevated beneath subduction zones. Upper mantle velocity anisotropy is regularly *SH*-fast on the down-dip side of subduction zones and at the CMB. The common co-location of strong anisotropy and high Q_{ISO} may result from decreased diffusion creep allowing for the preservation and formation of lattice-preferred orientation. Large magnitude high-

Q_{SV} anisotropy commonly occurs as thin slabs within high- Q_{ISO} anomalies underlying subduction zones. High- Q_{SH} anisotropy is more commonly found within the highly attenuating regions down-dip of subduction zones. This anisotropy would more likely result from a shape-preferred orientation (SPO) because LPO is inhibited by increased diffusion creep [Ashby, 1978; McNamara *et al.*, 2003], which also causes low- Q_{ISO} values [Gribb and Cooper, 2000].

Megaplumes and Spreading Ridges

Long-wavelength low- Q_{ISO} and low- V_{ISO} anomalies within the lower mantle correspond with regions of increased geoid height [Hager *et al.*, 1985] and hotspot activity under the Pacific and Africa. These large anomalies are observed to rise more than 1000 km above the CMB. Geodynamic investigations constrained by seismic velocity observations indicate that these anomalies are rising [Forte and Mitrovica 2001]. Due to their plume-like attributes, these anomalies are referred to as megaplumes [Wen *et al.*, 2001; Wen, 2002]. The Pacific megaplume is consistent with a weak vertically aligned anisotropy, implying vertical motion. The African megaplume is more consistent with fast- SH anisotropy, suggestive of horizontal motion or layering. However, both anisotropic signatures are small ($< 1\%$) and therefore poorly constrained. However, LPO anisotropy is unlikely in these regions as a result of high diffusion creep associated with low Q_{μ} , even if flow is strong [McNamara *et al.*, 2003].

Away from the East Pacific and Atlantic mid-ocean ridges, high- Q_{ISO} anomalies at depths between 400 and 1300 km thicken to over 1000 km, and increase in strength by over 10%. Near the mid-ocean ridges, the high- Q_{ISO} anomalies are gradually thinned and

replaced by low- Q_{ISO} anomalies (Figure 10). In the thinned region, communication between the upper and lower mantle is likely increased. Beneath the East Pacific Ridge, the Pacific superplume may extend from the core to the crust, as seen in Figure 6.10c. Beneath the Atlantic ridge, low- Q_{ISO} material may extend from the core to the crust, but the low- V_{ISO} anomaly is confined to the lower mantle beneath Africa (Figure 6.10d)

The differences between the two megaplumes are significant. The Pacific megaplume seems to rise across the entire mantle in a primarily vertical manner, largely unimpeded. However, the African megaplume is limited to the lower mantle beneath Africa, but seems to be connected to and feeding the spreading ridges in the Atlantic and Indian Oceans (Figure 10d). This was previously identified by *Romanowicz and Gung* [2002]. In this scenario, there would be significant horizontal flow at the top of the lower mantle associated with the African megaplume [*Behn et al.*, 2002], and this deflection could account for the fast- V_{SH} direction observed in the lower mantle beneath Africa.

Hotspots

Vigorous debate exists regarding the source depth of hotspots [*Ritsema et al.*, 1999; *Wolfe et al.*, 1997; *Foulger and Pearson* 2001]. While some hotspots are shallow upper-mantle features, others seem to be true mantle plumes that extend across the entire mantle [*Montelli et al.*, 2004]. The hotspot locations of *Steinberger* [2000] are overlain on the maps of V_S , Q_{μ} , and anisotropy (Figure 15). There are several distinct patterns that emerge; the most significant is that over 80% of all hotspots are located over low- Q_{ISO} D'' regions. More than 70% occur above low- Q_{ISO} regions in the transition zone. Approximately 60% occur overlying regions with low- V_{ISO} for both D'' and the transition

zone. Less than 30% of the hotspots occur above high- V_{SH} anisotropy in the transition zone. Less than 40% occur above high- Q_{SH} anisotropy in the transition zone or D". These statistics lead us to surmise that some hotspots are indeed likely to be linked to both upper and lower mantle processes. Simultaneous low values of Q_{ISO} and V_S suggest elevated temperatures, and the vertically-aligned anisotropy suggests vertical flow. The low Q_{μ} values found in regions with hotspot activity may also indicate lower viscosity values, which would be important for understanding upward material flow rates.

Q_{μ} and V_S anisotropy

There are two mechanisms for anisotropy; lattice-preferred orientation (LPO) and shape-preferred orientation (SPO) [Karato, 1998; Kendall, 2000]. SPO is a product of structural anisotropy, such as laminar melt sills. LPO is a product of mineral alignment in response to convective flow [McKenzie, 1979]. Under high stress or large grain size, dislocation creep encourages LPO development. Under low stress or small grain size, diffusion creep breaks down LPO, requiring SPO to explain strong anisotropy. Figure 6.9 demonstrates that Q_{μ} anisotropy and V_S anisotropy are much stronger near subduction, where stress is high, and grain size is likely to vary significantly [McNamara *et al.*, 2003]. Coincident high Q_{μ} and V_S may also be promoted by high stress, low temperature, or variable grain size.

The preferred mechanism of anisotropy for the majority of the mantle is LPO. However, shape preferred orientation is required to explain some anomalies, and has been called upon to explain anisotropy in D" [Kendall and Silver, 1998; Wysession *et al.*, 1999]. The co-location of large amplitude anisotropy with high- Q_{ISO} indicates increased

preference for dislocation creep over diffusion creep in giving rise to opportune conditions for LPO. Q_{μ} should increase as a result of larger grain dimensions [Jackson *et al.*, 2001]. Therefore, it follows that the fast direction should agree with the high- Q_{μ} direction due to LPO [Mutzsch *et al.*, 2003]. In fact, velocity anisotropy and attenuation anisotropy are loosely correlated ($R^2 = 0.38$) despite problems with amplitude and resolution under the current anisotropy calculation method. The highest amplitude anisotropy anomalies occur beneath subduction zones, where McNamara *et al.*, [2003] demonstrated that anisotropy should be strongest. The majority of non-subduction-zone lower mantle is largely isotropic and low- Q_{μ} , suggesting that high diffusion creep conditions may destroy LPO. Within the ultra-low- Q_{ISO} regions down-dip of subduction zones between 670 and 1400 km depth, high- V_{SH} and high- Q_{SH} anisotropy are observed. Due to either smaller grain size or elevated temperatures inferred from the ultra-low- Q_{ISO} , diffusion creep should dominate this region. Consequently our interpretation is that this anisotropy is likely due to SPO.

The finite strain computations of Becker *et al.*, [2003] demonstrate that vertically-aligned LPO should occur at the initiation of subduction and at mid-ocean ridges. Horizontally-aligned LPO should occur immediately down dip of subduction zones and with greater distance from spreading ridges. Consequently, the fast direction should be horizontal for the majority of the upper mantle. Within the uppermost mantle, the only resolvable anisotropy exhibits high-amplitude V_{SH} -fast anisotropy on the down-dip side of western Pacific subduction. The strongest resolvable V_{SV} -fast anisotropy in the upper mantle occurs up-dip of subduction. For Q_{μ} , this trend also exists, but with less certainty.

Conclusions

The long-wavelength global patterns of inverted V_S , Q_μ , and anisotropy are resolvable for the whole mantle from a set of teleseismic shear wave differential travel-time and attenuation data. The model presented here, VQM3DA, resolves high V_S , high Q_μ , and high amplitude anisotropy anomalies beneath subduction zones, and low V_S , low Q_μ , and low amplitude anisotropy beneath non-subduction zone regions. The observed pattern of V_S and Q_μ indicates a large degree of whole-mantle material flow beneath subduction zones. Beneath the East Pacific spreading ridge, whole-mantle low Q_μ , low V_S , and small amplitude V_{SV} -fast anisotropy anomalies are less well resolved, but observed nevertheless. The African megaplume also possesses low Q_μ and low V_S , but is confined to the lower mantle and has, if anything, V_{SH} -fast anisotropy that may be due to horizontal flow towards the Atlantic and Indian Ocean spreading ridges.

This study demonstrates that lateral Q_μ anomalies are significant in the lower mantle as well as the upper mantle. While Q_μ is much higher in the lower mantle, making it more difficult to resolve the anomalies, differential methods make such observations more accurate. In the future, more emphasis will be placed on observing attenuation with different phase pairs to increase the data coverage, number of crossing paths, and sensitivity to different depths. Once Frechet kernels are developed for differential attenuation, more accurate inversion techniques may be possible. A global model of attenuation would greatly benefit from simultaneous inversion of surface wave and body wave amplitudes.

Acknowledgements: The inversions described in this document were greatly improved using advice and subroutines supplied by Guy Masters. Conversations with the following individuals greatly improved the interpretation of this manuscript; Shun Karato, Shun Karato, Eiji Ohtani, Greg Hirth, Dave Kohlstedt, Steven Jacobsen, Neil Ribe, Joseph Smyth, Tom Sharp, and Jason Phipps Morgan. The data were provided by the IRIS DMS. We thank Emily Carter, Tracy Portle, Juliana Rakosky and Kurt Solander for assisting with data processing. This research was supported under NSF grant EAR-0207751.

References

- Angel, R. J., D. J. Frost, N. L. Ross, and R. Hemley (2001), Stabilities and equations of state of dense hydrous magnesium silicates, *Phys. Earth Planet Inter.*, *127*, 181-196.
- Antolik, M., Y. J. Gu, G. Ekstrom, and A. M. Dziewonski (2004), J362D28: a new joint model of compressional and shear velocity in the Earth's mantle, *Geophys. J. Int.*, *153*, 443-466.
- Ashby, M.F.a.V., R.A. (1978) Micromechanisms of flow and fracture, and their relevance to the rheology of the upper mantle., *Phil. Trans. R. Soc. Lond.*, *288*, 59-95, 1978.
- Bassin, C., Laske, G. & Masters, G., 2000. The current limits of resolution for surface wave tomography in North America, *EOS*, *81*, F897, also available at mahi.ucsd.edu/Gabi/crust2.html.
- Becker, T.W., and L. Boschi (2002), A comparison of tomographic and geodynamic mantle models, *Geochemistry Geophysics Geosystems*, *3*.
- Becker, T.W., J.B. Kellogg, G. Ekstrom, and R.J. O'Connell (2003), Comparison of azimuthal seismic anisotropy from surface waves and finite strain from global mantle-circulations models, *Geophys. J. Int.*, *155*, 696-714.
- Behn, M. D., C. P. Conrad, and P. G. Silver (2004), Detection of upper mantle flow associated with the African Superplume, *Earth Planet. Sci. Lett.*, *224*, 259-274.
- Bhattacharyya, J., G. Masters, and P. M. Shearer (1996), Global lateral variations of shear wave attenuation in the upper mantle, *J. Geophys. Res.*, *101*, 22,273-22,289.
- Bolfan-Casanova, N., S. Mackwell, H. Kappler, C. McCammon, and D. C. Rubie (2002), Pressure dependence of H solubility in magnesiowüstite up to 25 GPa: Implications for the storage of water in the Earth's lower mantle, *Geophys. Res. Lett.*, *29*, 89-92.
- Bolfan-Casanova, N., H. Kappler, and D. C. Rubie (2003), Water partitioning at 660 km depth and evidence for very low water solubility in magnesium silicate perovskite, *Geophys. Res. Lett.*, 1905, doi:10.1029/2003GL017182.
- Boschi, E. (2003), Measures of resolution in global body wave tomography, *Geophys. Res. Lett.*, *30* (19), doi:10.1029/2003GL018222.
- Brana, L., and G. Helffrich (2004), A scattering region near the core-mantle boundary under the North Atlantic, *Geophys. J. Int.*, *158*, 625-636.
- Bunge, H.-P., Richards, M.A., Lithgow-Bertelloni, C., Baumgardner, J.R., Grand, S.P. & Romanowicz, B., 1998. Time scales and heterogeneous structure in geodynamic earth models, *Science*, *280*, 91-95.
- Castle, J. C., and R. D. van der Hilst (2003), Searching for seismic scattering off mantle interfaces between 800 km and 2000 km depth, *J. Geophys. Res.*, *108*, pp. ESE 13-1, CiteID 2095, DOI 10.1029/2001JB000286.
- Cooper, R. F. (2002), Seismic wave attenuation: Energy dissipation in viscoelastic crystalline solids, in *Plastic Deformation of Mineral and Rocks*, S.-i. Karato and H.-R. Wenk, eds., *Rev. Mineral. Geochem.*, *51*, 253-290.
- Cormier, V. F. (2000), D" as a transition in the heterogeneity spectrum of the lowermost mantle, *J. Geophys. Res.*, *105*, 16,193-16,205.

- Crichton, W. A., and N. L. Ross (2002), Equation of state of dense hydrous magnesium silicate phase A, $\text{Mg}_7\text{Si}_2\text{O}_8(\text{OH})_6$, *Amer. Mineralogist*, 87, 333-338.
- Dahlen, A., Hung, S.H. & Nolet, G., 2000. Fréchet Kernels for finite-frequency traveltimes I. Theory, *Geophys. J. Int.*, 141, 157–174.
- Dziewonski, A. M. 1984. Mapping the lower mantle: determination of lateral heterogeneity in P velocity up to degree and order 6. *J. Geophys. Res.* 89:5929-52
- Ekstrom, G. & Dziewonski, A. M (1998). The unique anisotropy of the Pacific upper mantle. *Nature* 394, 168–172.
- Fisher, J.L., M.E. Wysession, and K.M. Fischer (2003), Small-scale lateral variations in D" attenuation and velocity structure, *Geophys. Res. Lett.*, 30, doi:10.1029/2002GL016179.
- Flanagan, M. P., and D. A. Wiens (1990), Attenuation structure beneath the Lau back-arc spreading center from teleseismic S phases, *Geophys. Res. Lett.*, 17, 2117-2120.
- Forte, A. M., and J.X. Mitrovica (1996), New inferences of mantle viscosity from joint inversion of long-wavelength mantle convection and post-glacial rebound data, *Geophys. Res. Lett.* 23, 1147-1150.
- Forte, A. M., and J.X. Mitrovica (2001), Deep-mantle high-viscosity flow and thermochemical structure inferred from seismic and geodynamic data, *Nature*, 410, 1049-1056.
- S. P Grand, R. D. van der Hilst, S. Widiyantoro, (1997) Global seismic tomography: a snapshot of convection in the earth, *Geol. Soc. Am. Today* 7, 1.
- Garnero, E., J. Revenaugh, Q. Williams, T. Lay, and L. Kellogg (1998), Ultra-low velocity zone at the core-mantle boundary, in *Observational and Theoretical Constraints on the Core-Mantle Boundary Region*, edited by M. Gurnis, M.E. Wysession, B.A. Buffett, and E. Knittle, AGU, Washington D.C..
- Garnero, E.J. (2000), Heterogeneity of the Lowermost Mantle, *Annu. Rev. Earth Planet. Sci.*, 28 (1), 509-37.
- Getting, I.C., S.J. Dutton, P.C. Burnley, S. Karato (1997), and H.A. Spetzler, Shear attenuation and dispersion in MgO, *Phys. Earth Planet. Int.*, 99, 249-257.
- Grand, S.P. (1994), Mantle shear structure beneath the Americas and surrounding oceans, *J. Geophys. Res.*, 99, 11,591-11,621.
- Grand, S.P., R.D. van der Hilst, and S. Widiyantoro (1997), Global seismic tomography: a snapshot of convection in the Earth, *Geol. Soc. Am. Today*, 7, 1–7.
- Grand, S. P. (2002), Mantle shear-wave tomography and the fate of subducted slabs, *Phil. Trans., Math. Phys. Eng. Sci.*, 360, 2475-2491.
- Green, D.H., R.F. Cooper, and S. Zhang (1990), Attenuation spectra of olivine/basalt partial melts: Transformation of Newtonian creep response, *Geophys. Res. Lett.*, 17, 2097-2100.
- Gribb, T.T., and R.F. Cooper, The effect of an equilibrated melt phase on the shear creep and attenuation behavior of polycrystalline olivine, *Geophys. Res. Lett.*, 27 (15), 2341-2344, 2000.
- Gung, Y., M. Panning, and B. Romanowicz 2003. Global anisotropy and the thickness of continents, *Nature*, 422, 707-711.
- Gung, Y.C., and B. Romanowicz, Q tomography of the upper mantle using three component long period waveforms., *Geophys. J. Int.*, *In press*, 2004.
- Hager, B.H., R.W. Clayton, M.A. Richards, W. Robert, and A.M. Dziewonski (1985),

- Lower mantle heterogeneity, dynamic topography and the geoid, *Nature*, 313, 541-545.
- Hager, B. H., and M.A. Richards (1989), Long-wavelength variations in Earth's geoid: Physical models and dynamical implications, *Phil. Trans. R. Soc. Lond.* A328, 309-327.
- Hedlin, M. A. H., P. M. Shearer, and P. S. Earle (1997), Seismic evidence for small-scale heterogeneity throughout the Earth's mantle, *Nature*, 387, 145-150.
- Helfrich, G. (2002), Chemical and seismological constraints on mantle heterogeneity, *Phil. Trans.: Math., Phys. And Eng. Sci.*, 360, 2493 – 2505.
- Helmberger, D., S. Ni, L. Wen, and J. Ritsema (2000), Seismic evidence for ultralow-velocity zones beneath Africa and eastern Atlantic, *J. Geophys. Res.*, 105, 23865-23878.
- Hirth G. and D. L. Kohlstedt (1996), Water in the oceanic upper mantle; implications for rheology, melt extraction and the evolution of the lithosphere, *Earth Planet. Sci. Lett.*, 144, 93-108.
- Iwamori, H., and Chau (2000), The water in the slab and the material circulation in the mantle, *Journal of Geography*, 109, 495-496.
- Inoue, T., D. J. Wiedner, P. A. Northrup, and J. B. Parise (1998), Elastic properties of hydrous ringwoodite (γ -phase) in Mg_2SiO_4 , *Earth Planet. Sci. Lett.*, 160, 107-113.
- Irifune, T., N. Kubo, M. Isshiki, and Y. Yamasaki (1998), Phase transformations in serpentine and transportation of water into the lower mantle *Geophys. Res. Lett.*, 25, 203-206.
- Jackson, I. (2000), Laboratory Measurements of Seismic Wave dispersion and Attenuation: Recent Progress. In *Earth's Deep Interior: Mineral Physics and Tomography from the Atomic to the Global Scale*, AGU Geophysical Monograph Service, vol.117, S. Karato et al (eds), pp. 265-289.
- Jackson, I., M. S. Paterson, and J. D. Fitz Gerald (1992), Seismic wave attenuation in Aheim dunite: an experimental study, *Geophys. J. Int.*, 108, 517-534.
- Jackson, I., J. D. Fitz Gerald, U. H. Faul, and B. H. Tan (2001), Grain-size sensitive seismic wave attenuation in polycrystalline olivine, *J. Geophys. Res.*, 107, 2360, doi: 10.1029/2001JB001225.
- Kaneshima, S., and G. Helfrich (1998), Detection of lower mantle scatterers northeast of the Mariana subduction zone using short-period array data, *J. Geophys. Res.*, 103, 4825-4838.
- Kaneshima, S., and G. Helfrich (1999), Dipping Low-Velocity Layer in the Mid-Lower Mantle: Evidence for Geochemical Heterogeneity, *Science*, 283, 1888-1892.
- Karason, H., and R. D. van der Hilst (2001), Tomographic imaging of the lowermost mantle with differential times of refracted and diffracted core phases (*PKP, Pdiff*), *J. Geophys. Res.*, 106, 6569-6587.
- Karato, S.-i (1997). On the separation of crustal component from subducted oceanic lithosphere near the 660-km discontinuity, *Phys. Earth Planet. Inter.*, 99, 103-111.
- Karato, S.-i. (2003), Mapping water content in the upper mantle, in *Inside the Subduction Factory*, J.M. Eiler ed., *Geophys. Monogr.*, 138, 135-152.

- Karato, S.-i. (2005), Microscopic models for the effects of hydrogen on physical and chemical properties of earth materials, In *Beyond plate tectonics*, ed. by D. A. Yuen, S. Maruyama, S. Karato, and B. F. Windley, in press.
- Karato, S.-i., and H. Jung (1998), Water, partial melting and the origin of the seismic low velocity and high attenuation zone in the upper mantle, *Earth. Planet. Sci. Lett.*, *157*, 193-207.
- Kellogg, L.H., and S.D. King (1993), Effect of mantle plumes on the growth of D' by reaction between the core and mantle, *Geophys. Res. Lett.*, *20*, 379-382.
- Kendall, J.-M. and P.G. Silver (1998) Constraints from seismic anisotropy on the nature of the lowermost mantle, *Nature*, *381*, 409-412.
- Kendall, J.-M. and P.G. Silver (1998), Investigating causes of D'' anisotropy, in *The Core Mantle Boundary Region*, edited by M. Gurnis, M.E. Wyssession, E. Knittle, and B.A. Buffett, pp. 97-118., AGU, Washington D.C..
- Kennett, B., S. Widiyantoro, and R.D. van der Hilst (1998), Joint seismic tomography for bulk sound and shear wave speed in the Earth's mantle, *J. Geophys. Res.*, *103*, 12,469-12,494.
- Kirby, S. H., S. Stein, E. A. Okal, and D. C. Rubie (1996), Metastable mantle phase transformations and deep earthquakes in subducting oceanic lithosphere, *Rev. of Geophys.*, *34*, 261-306.
- Knittle, E., and R. Jeanloz (1991), Earth's core-mantle boundary: results of experiments at high pressure and temperature, *Science*, *251*, 1438-1443.
- Kuo, B.-Y., D.W. Forsyth, and M.E. Wyssession (1987), Lateral heterogeneity and azimuthal anisotropy in the North Atlantic determined from SS-S differential travel times, *J. Geophys. Res.*, *92* (B7), 6421-6436.
- Lawrence, J. F., and M. E. Wyssession (2005a), QLM9: A new radial quality factor (*Q*) model for the mantle, *Earth Planet. Sci. Lett.*, in press.
- Lawrence, J. F., and M. E. Wyssession (2005b), A large seismic attenuation anomaly beneath Asia: Possible evidence for elevated hydration in the lower mantle, *Geophys. Res. Lett.*, in review.
- T. Lay, Q. Williams, E. J. Garnero, L. Kellogg, M. Wyssession (1998), Seismic wave anisotropy in the D'' region and its implications, in *The Core-Mantle Boundary Region*, M. Gurnis, M. E. Wyssession, E. Knittle, B. A. Buffett, Eds., American Geophysical Union, Washington, DC, , pp. 219–318.
- Lay, T., and D.V. Helmberger (1983), A lower mantle S-wave triplication and the shear velocity structure of D'', *Geophys. J. R. astro. Soc.*, *75*, 799-837.
- Litasov, K., E. Ohtani, F. Langenhorst, H. Yurimoto, T. Kubo, and T. Kondo (2003), Water solubility in Mg-perovskites and water storage capacity in the lower mantle, *Earth Planet. Sci. Lett.*, *211*, 189-203.
- Lithgow-Bertelloni, C., and M.A. Richards (1995), Cenozoic plate driving forces, *Geophys. Res. Lett.*, *22* (11), 1317-1320.
- Lithgow-Bertelloni, C., and M.A. Richards (1998), The dynamics of Cenozoic and Mesozoic plate motions, *Rev. Geophys.*, *36*, 27–78.
- Li, X.D., and B. Romanowicz, Global mantle shear-velocity model developed using nonlinear asymptotic coupling theory, *J. Geophys. Res.*, *101*, 22,245-22,272, 1996.

- Lin, J.-F., E. Gregoryanz, V. V. Struzhkin, and M. Somayazulu (2005), Melting behavior of H₂O at high pressures and temperatures, *Geophys. Res. Lett.*, *32*, L11306, doi:10.1029/2005GL022499.
- Liu, L.-G. (1986), Phase transformations in serpentine at high pressures and temperatures and implications for subducting lithosphere, *Phys. Earth Planet. Inter.*, *42*, 255-262.
- Liu, L.-G. (2002), Are hydrous phases more compressible? Implications for high-velocity zones in the deep mantle, *Geophys. J. Int.*, *149*, 37-43.
- Mackwell, S. J., D. L. Kohlstedt, and M. S. Paterson (1985), The role of water in the deformation of olivine single crystals, *J. Geophys. Res.*, *90*, 11319-11334.
- Masters, G., T.H. Jordan, P.G. Silver, and F. Gilbert, (1982). Aspherical earth structure from fundamental spheroidal mode data, *Nature*, *298*, 609-13.
- Masters, G., S. Johnson, G. Laske, and H. Bolton (1996), A shear-velocity model of the mantle, *Phil. Trans. R. Soc. Lond. A*, *354*, 1385-1411.
- Masters, G., G. Laske, H. Bolton, and A. M. Dziewonski (2000), The relative behavior of shear velocity, bulk sound speed, and compressional velocity in the mantle: Implications for chemical and thermal structure, in *Earth's Deep Interior*, S. Karato, A. M. Forte, R. C. Liebermann, G. Masters and L. Stixrude, eds., AGU Monograph 117, AGU, Washington D.C..
- Maultzsch, S., S. Horne, S. Archer, and H. Burkhardt (2003), Effects of an anisotropic overburden on azimuthal amplitude analysis in horizontal transverse isotropic media, *Geophys. Prosp.*, *51*, 61-74.
- McNamara, A. K., P. E. van Keken and S. Karato (2003), Development of finite strain in the convecting lower mantle and its implications for seismic anisotropy, *J. Geophys. Res.*, *108*, doi:10.1029/2002JB001970.
- Megnin, C., H.-P. Bunge, B. Romanowicz (1997), and M.A. Richards, Imaging 3-D spherical convection models: What can seismic tomography tell us about mantle dynamics?, *Geophys. Res. Lett.*, *24*, 1299-1302.
- Megnin, C., and B. Romanowicz (2000), The shear velocity structure of the mantle from the inversion of body, surface and higher modes waveforms, *Geophys. J. Int.*, *142*, 709-726.
- Mei, S., and D. L. Kohlstedt (2000), Influence of water on plastic deformation of olivine aggregates 1. Diffusion creep regime, *J. Geophys. Res.*, *105*, 21457-21470.
- Montagner, J.P., and T. Tanimoto (1990), Global anisotropy in the upper mantle inferred from the regionalization of phase velocities, *J. Geophys. Res.*, *95*, 4797-4819.
- Montelli, R., G. Nolet, F. A. Dahlen, G. Masters, E. R. Engdahl, and S.-H. Hung (2004), Finite frequency tomography reveals a variety of plumes in the mantle, *Science*, *303*, 338-343.
- Murakami, M., K. Hirose, H. Yurimoto, S. Nakashima, and N. Takafuji (2002), Water in Earth's lower mantle *Science*, *295*, 1885-1887.
- Nataf, H.C., I. Nakanishi, D.L. Anderson, (1986). Measurements of mantle wave velocities and inversion for lateral heterogeneities and anisotropy, 3. Inversion. *J. Geophys. Res.*, *91*, 7261-7307.
- Ni, S., D. Helmberger, and J. Tromp (2005), Three-dimensional structure of the African superplume from waveform modelling, *Geophys. J. Int.*, *161*, 283-294.

- Nishimura, C.E., and D.W. Forsyth (1989), The anisotropic structure of the upper mantle in the Pacific, *Geophys. J. Int.*, *96*, 203-229.
- Nolet, G. (1987), Seismic wave propagation and seismic tomography, in *Seismic Tomography*, G. Nolet, ed., Reidel, Dordrecht, 1-23.
- Ohtani, E. (2005), Water in the mantle, *Elements*, *1*, 25-30.
- Ohtani, E., H. Mitzobata, Y. Kudoh, and T. Nagase (1997), A new hydrous silicate, a water reservoir, in the upper part of the lower mantle, *Geophys. Res. Lett.*, *24*, 1047-1050.
- Paige, C.C., and M. A. Saunders (1982), LSQR: An algorithm for sparse linear equations and sparse least squares, *TOMS*, *8*, 43-71.
- Peacock, S. (1990), Fluid processes in subduction zones, *Science*, *248*, 329-337.
- Reid, F.J.L. J.H. Woodhouse, and H.J. van Heijst (2001), Upper mantle attenuation and velocity structure from measurements of differential S phases, *Geophys. J. Int.*, *145*, 615-630.
- Ricard, Y., M.A. Richards, C. Lithgow-Bertelloni, and Y.L. Stunff (1993), A geodynamic model of mantle density heterogeneity, *J. Geophys. Res.*, *98* (B12), 21,895-21,910.
- Ritsema, J., and H. J. Van Heijst (2000), Seismic imaging of structural heterogeneity in Earth's mantle: Evidence for large-scale mantle flow, *Science Progress*, *83*, 243-259.
- Romanowicz, B. (1995), A global tomographic model of shear attenuation in the upper mantle, *J. Geophys. Res.*, *100*, 12,375-12,394.
- Romanowicz, B., and J. J. Durek (2000), Seismological constraints on attenuation in the earth: A review, in *Earth's Deep Interior*, AGU Geophysical Monograph, *117*, 265-289.
- Romanowicz, B. and Y. Gung (2002), Superplumes from the Core-Mantle Boundary to the Lithosphere: Implications for Heat Flux, *Science*, *296*, 513 – 516.
- Roth, E.G., D.A. Wiens, and D. Zhao (2000), An empirical relationship between seismic attenuation and velocity anomalies in the upper mantle, *Geophys. Res. Lett.*, *27* (5), 601-604.
- Roth, E.G., D.G. Wiens, L.M. Dorman, J. Hildebrand, and S.C. Webb (1999), Seismic attenuation tomography of the Tonga- Fiji region using phase pair methods, *J. Geophys. Res.*, *104*, 4795-4809.
- Russell, S., L. T., and E.J. Garnero (1999), Small scale lateral shear velocity and anisotropy heterogeneity near the core-mantle boundary beneath the central Pacific 206 imaged using broadband ScS waves, *J. Geophys. Res.*, *104*, 13181-13199.
- Sato, H., I. S. Sacks, T. Murase, G. Muncill, and H. Fukuyama (1989), Qp-melting temperature relation in peridoite at high pressure and temperature: attenuation mechanism and implications for the mechanical properties of the upper mantle, *J. Geophys. Res.*, *94*, 10647-10661.
- Selby, N.D., and J.H. Woodhouse (2000), Controls on Rayleigh wave amplitudes: attenuation and focusing, *Geophys. J. Int.*, *142*, 933-940.
- Selby, N.D., and J.H. Woodhouse (2002), The Q structure of the upper mantle: Constraints from Rayleigh wave amplitudes, *J. Geophys. Res.*, *107* (B5),

- doi:10.1029/2001JB000257.
- Shieh, S. R., H.-k. Mao, R. J. Hemley, and L. C. Ming (1998), Decomposition of phase D in the lower mantle and the fate of dense hydrous silicates in subducting slabs, *Earth Planet. Sci. Lett.*, *159*, 13-23.
- Sipkin, S.A., and T.H. Jordan (1979), Frequency dependence of QScS, *Bull. Seis. Soc. Am.*, *69*, 1055-1079.
- Smyth, J. R., C. M. Holl, D. J. Frost, and S. D. Jacobsen (2004), High pressure crystal chemistry of hydrous ringwoodite and water in the Earth's interior, *Phys. Earth Planet. Int.*, *143*, 271-278.
- Solomatov, V.S., and L. Moresi (2002), Small-scale convection in the D" layer, *J. Geophys. Res.*, *107*, doi:10.1029/2000JB000063.
- Spetzler, H.A., J.C. Sivaji, O. Nishizawa, and Y. Fukushima (2002), A test of ray theory and scattering theory based on a laboratory experiment using ultrasonic waves and numerical simulation by finite-difference method, *Geophys J Int*, *148*, 165-178.
- Steinberger, B.M. (2000), Slabs in the lower mantle-results of dynamic modelling compared with tomographic images and geoid, *J. Geophys. Res.*, *78*, 3321-3333.
- Steinberger, B. M., and A.R. Calderwood (2001), Mineral physics constraints on viscous flow models of mantle flow, *J. Conf. Abs.*, *6*, 2001.
- Su, W.-J., and A.M. Dziewonski (1997), Simultaneous inversion for 3-D variations in shear and bulk velocity in the mantle, *Phys. Earth Planet. Inter.*, *100*, 135 –156.
- Venkataraman, A., A.A. Nyblade, and J. Ritsema (2004), Upper mantle Q and thermal structure beneath Tanzania, East Africa from teleseismic P wave spectra, *Geophys. Res. Lett.*, *Submitted*.
- VanDecar, J.C., and R.S. Crosson (1990), Determination of teleseismic relative phase arrival times using multi-channel cross correlation and least squares, *Bull. Seism. Soc. Am.*, *80*, 150-169.
- van der Hilst, R.D., S. Widiyantoro, E.R. Engdahl (1997), Evidence for deep mantle circulation from global tomography, *Nature*, *386*, 578-584.
- Van der Meijde, M., F. Marone, D. Giardini, and S. Van der Lee (2003), Seismic Evidence for Water Deep in Earth's Upper Mantle, *Science*, *300*, 1556-1558.
- Warren, L. and P. M. Shearer (2002), Mapping lateral variations in upper mantle attenuation by stacking *P* and *4* spectra, *J. Geophys. Res.*, *107*, doi:10.1029/2001JB001195.
- Webb, S., I. Jackson, and J. Fitz Gerald (1999), Viscoelasticity of the titanate Perovskites CaTiO₃ and SrTiO₃ at high temperature, *Phys. Earth Planet. Int.* (115), 259- 291.
- Wen, L. (2002), An SH hybrid method and shear velocity structures in the lowermost mantle beneath the central Pacific and South Atlantic Oceans, *J. Geophys. Res.*, *107*, pp. ESE 4-1, CiteID 2055, DOI 10.1029/2001JB000499.
- Wen, L., P. Silver, D. James, and R. Kuehnel (2001), Seismic evidence for a thermo-chemical boundary at the base of the Earth's mantle, *Earth Planet. Sci. Lett.*, *189*, 141-153..
- Woodhouse, J. H., Dziewonski, A. M. (1984). Mapping the upper mantle: three-dimensional modeling of earth structure by inversion of seismic waveforms. *J. Geophys. Res.* *89*:5953-86.
- Woodhouse, J. H., Dziewonski, A. M. (1989), Seismic modelling of the Earth's

- largescale three-dimensional structure. *Philos.Trans. R. Soc. London Ser. A* 328: 291-308.
- Wookey, J., J.M. Kendall, and G. Rumpker (2005) Lowermost mantle anisotropy beneath the north Pacific from differential S-ScS splitting, *Geophys. J. Int.*, 161, 829-838.
- Wysession, M.E., K.M. Fischer, G.I. Al-eqabi, P.J. Shore, and I. Gurari (2001), Using MOMA Broadband Array ScS-S Data to Image Smaller-Scale Structures at the Base of the Mantle, *Geophysical Research Letters*, 28 (5), 867-870.
- Wysession, M.E., A. Langenhorst, M.J. Fouch, K.M. Fischer, and G. Al-eqabi (1999), Lateral variations in compressional/shear velocities at the base of the mantle, *Science*, 284, 120–25.
- Zhang, S., and S.-I. Karato (1995), Lattice preferred orientation of olivine aggregates deformed in simple shear, *Nature*, 375, 774-777.
- Zhao, L., T.H. Jordan, and C.H. Chapman (2000), Three-dimensional Frechet differential kernels for seismic delay times, *Geophys. J. Int.*, 141, 558-576.

Table 1: Phase pair data

Phase Pair	Tangential	Radial
<i>ScS-S</i>	23,759	21,143
<i>sScS-sS</i>	5,746	4,968
<i>SS-S</i>	20,518	17,603
<i>sSS-sS</i>	2,286	1,972
<i>SKS-S</i>	0	3,627
<i>ScS-SS</i>	19,974	17,472
<i>S</i>	21,151	20,116
TOTAL	93,434	86,901

Figures:

Figure 1: Maps of a) broadband stations and b) earthquake locations used in this study.

Figure 2: There is excellent agreement for both amplitude and locality between the checkerboard a) input and b) inverted anomalies. The size of the blocks are 60° on the left side of the figure, and 36° on the right side. This figure shows checkerboard tests for only the tangential component of Q_μ at six depths, but the resolution is nearly identical (due to similar datasets) for radial component and velocity inversions as well.

Figure 3: The geometric relationship between tangential (T), radial (R), vertical (SV), and horizontal (SH) particle motions as a function of incidence angle (i).

Figure 4: The resolution tests with checkerboard wavelengths shorter than 36° lead to high misfit between input and inverted models. From the 36° -wavelength checkerboard test shown here it is possible to see where resolution is strong and where it is weak.

Figure 5: Lateral cross-sections through the 3D isotropic velocity model. Values are shown as percentage perturbations from radial PREM values [*Dziewonski and Anderson, 1981*].

Figure 6: Lateral cross-sections through the 3D isotropic Q_μ model. Values are shown as percentage perturbations from radial QLM9 values [*Lawrence and Wysession,*

2005a]. Both the attenuation and velocity (Figure 5) models are made using the same data set.

Figure 7: Lateral cross-sections through the 3D velocity anisotropy model, found using Equations 4 and 5. Positive (red) values represent fast V_{SH} relative to V_{SV} .

Figure 8: Lateral cross-sections through the 3D attenuation anisotropy model. Positive (red) values represent high Q_{SH} relative to Q_{SV} .

Figure 9: 360° vertical profile demonstrating the variation between isotropic velocity, isotropic quality factor, velocity anisotropy, and quality factor anisotropy anomalies near and away from subduction zones. Note the large magnitude of the anomalies in the northern hemisphere, where the profile goes through subduction zones, as opposed to the southern hemisphere.

Figure 10: Vertical profile demonstrating the variation between isotropic velocity and isotropic quality factor anomalies for several regions; a) Northwest Pacific subduction; b) Farallon subduction; c) Pacific megaplume; d) African megaplume. The location of each profile is shown on the map (e) at the bottom left. Spreading ridges are marked by black triangles and subduction zones are marked by white triangles. The direction of subduction and spreading are marked by the arrows. The open circles are possible hotspot locations [Steinberger, 2000].

Figure 11: Comparison of VQM3DA with other models: a) quality factor anomalies with QRLW8 [Gung and Romanowicz, 2004] for the upper mantle, b) isotropic velocity with SB4L18 [Masters et al., 2000] for upper and lower mantle, and c) anisotropic velocity for the upper and lower mantle compared to SAW16B16AN [Gung et al., 2003; Panning et al., 2003].

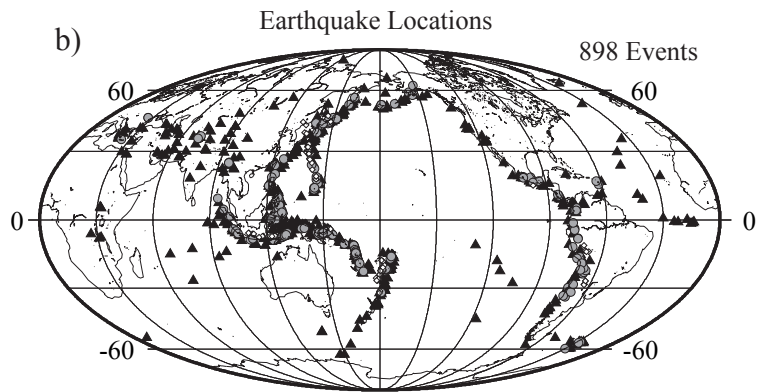
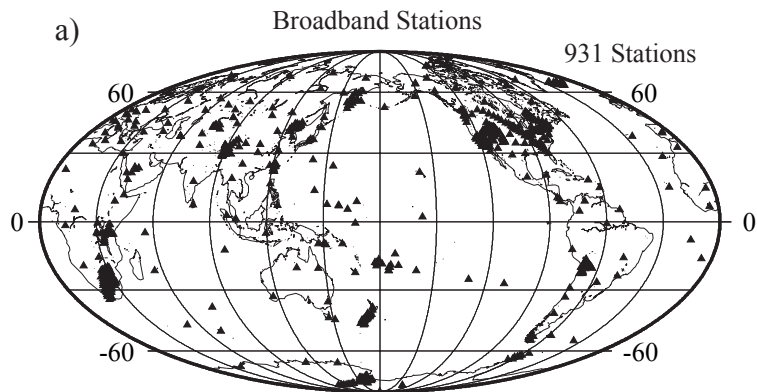
Figure 12: The radial model of velocity anisotropy compared to that of PREM (dashed line) [Dziewonski and Anderson, 1981] and SAW16B16AN (thin black line) [Gung et al., 2003; Panning et al., 2003].

Figure 13: Variation in temperature (dashed) and water content (solid line) have differing effects on velocity and attenuation ($1/Q_\mu$). This figure was computed using equations by Karato [2003]. Temperature increases the seismic velocity much more than water does for equivalent levels of attenuation. Therefore, the comparison between attenuation and velocity provides a method for distinguishing between thermal and water concentration anomalies. Alternate methods (e.g., grain size, chemical variation) must be required to cause large low-velocity variations with little increase in attenuation.

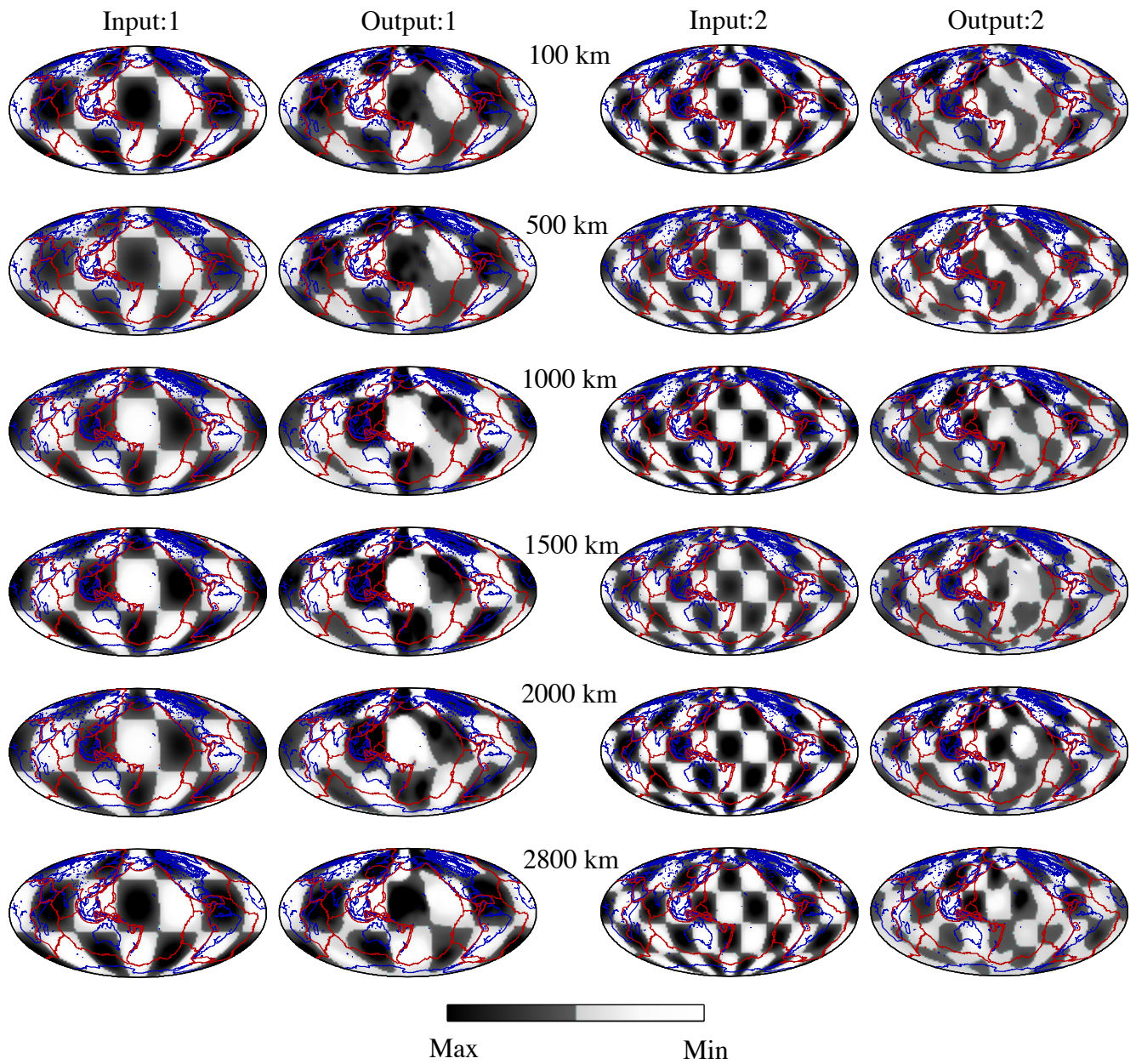
Figure 14: Vertical profiles through the Q_μ model illustrate the 3-D structure of western Pacific subduction and the East Asian low- Q_μ anomaly. The southernmost profile is illustrated with a cartoon of a possible flow pattern of water. Water may

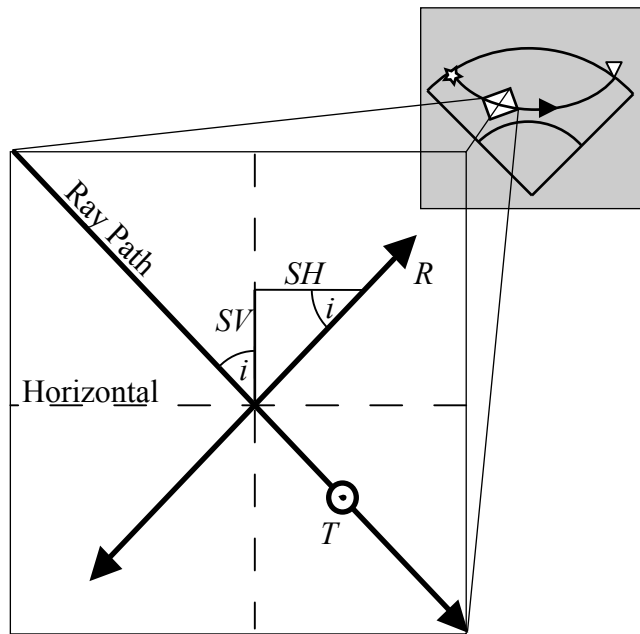
flow down (green) into the mantle a) in hydrous minerals within the slab, b) in hydrous minerals pulled down with the slab, or c) as interstitial H₂O pulled down with the slab. Once water leaves the slab d) through dehydration (blue) it may e) percolate up through the lower mantle as interstitial H₂O and saturate lower mantle minerals, f) reabsorb into transition zone, or g) continue convecting within the lower mantle. The locations of the profiles are shown on the map to the right.

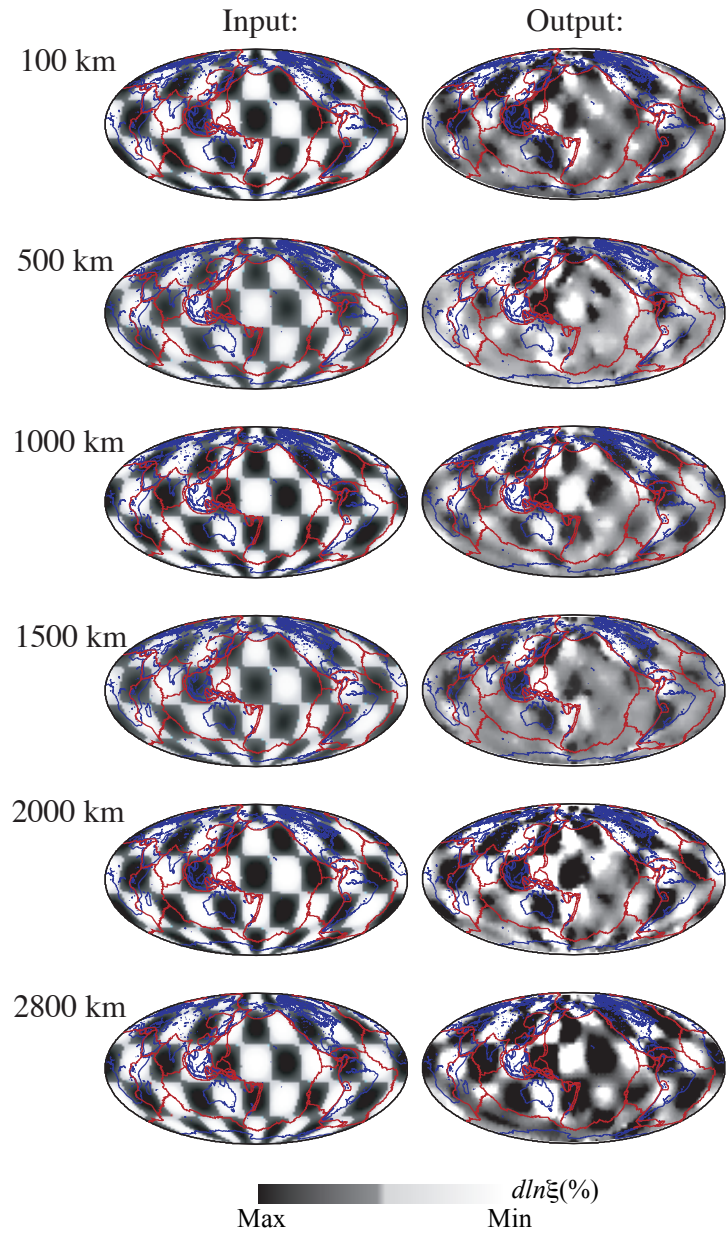
Figure 15: The hotspots of *Steinberger* [2000] are overlain on maps of a) isotropic shear velocity (V_S) b) quality factor (Q_μ), c) anisotropic velocity (ξ_V), and d) anisotropic quality factor (ξ_Q) at a depth of 500 km, in the upper mantle (top), and 2800 km, in the lower mantle (bottom).



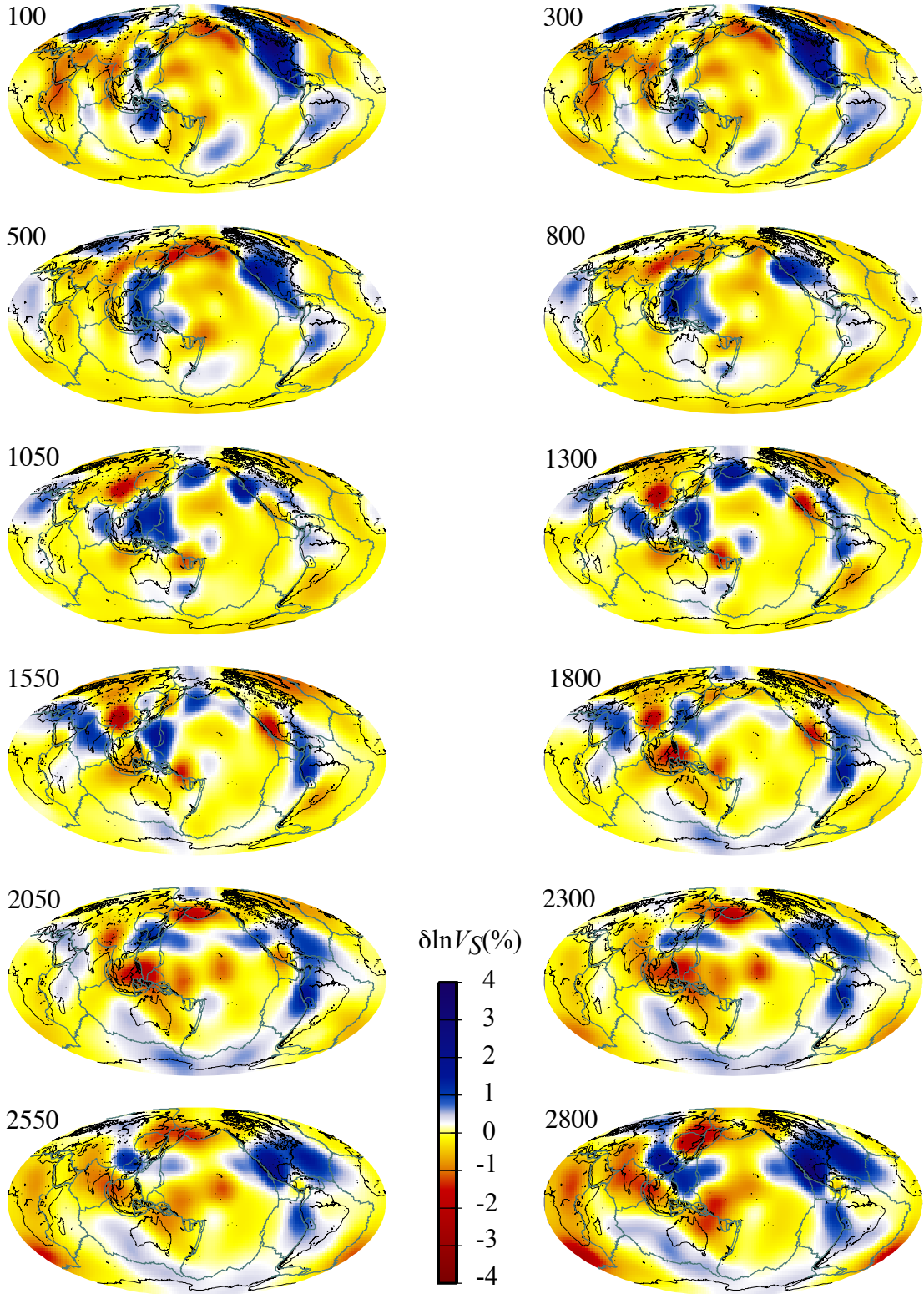
Deep: ◊ (> 300 km) Intermediate: ○ Shallow: ▲ (< 75 km)



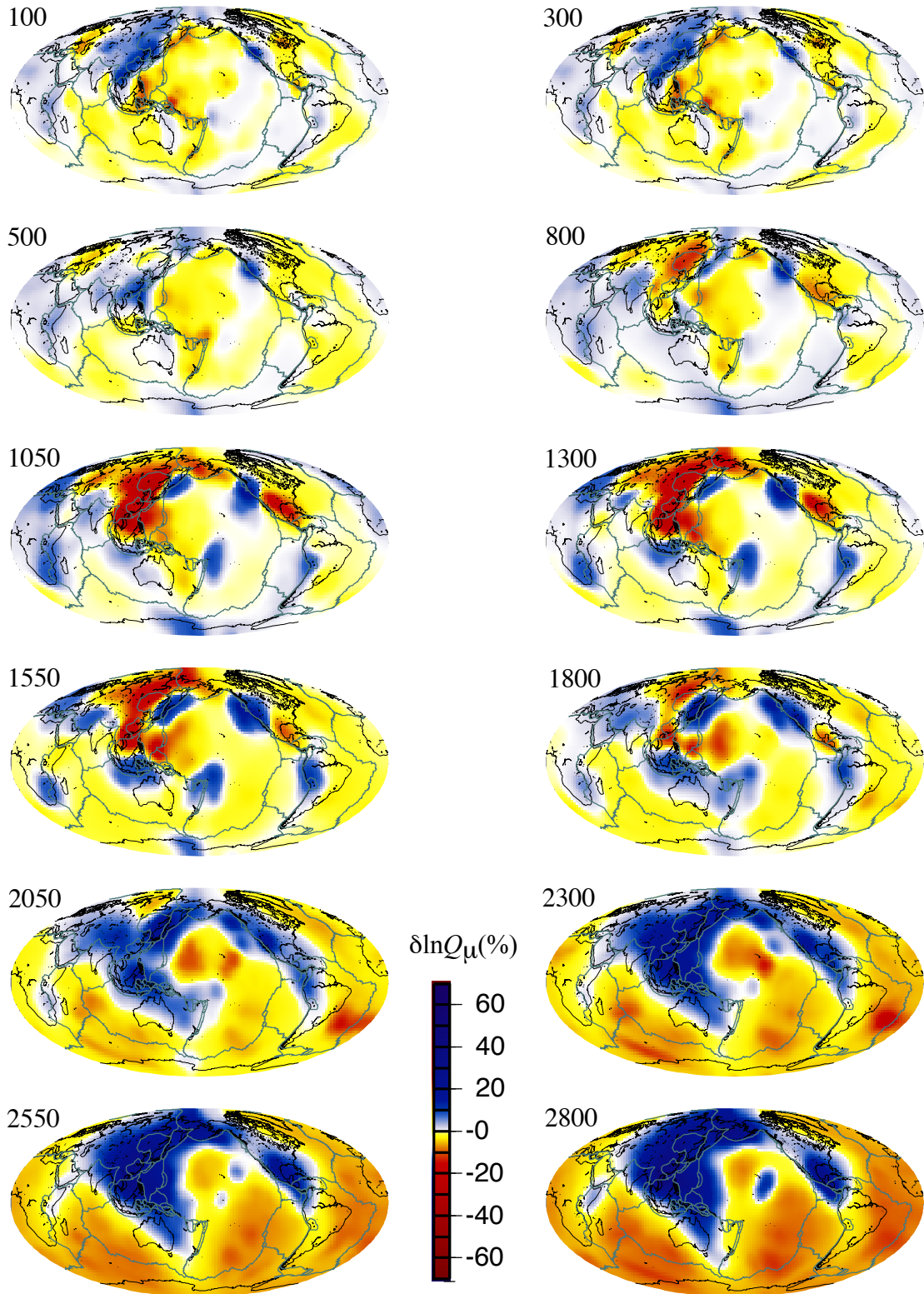




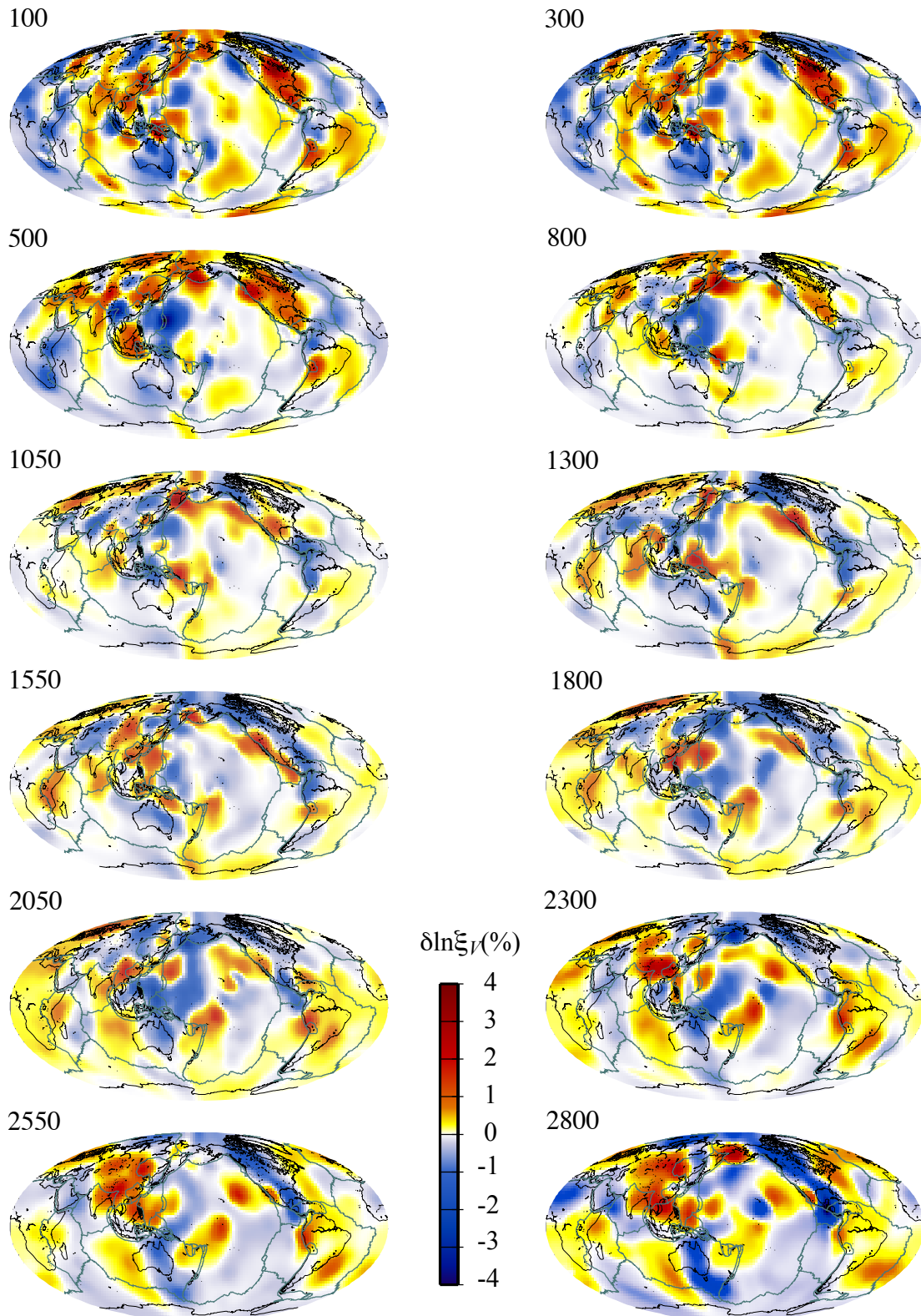
VQM3DA: Isotropic Velocity



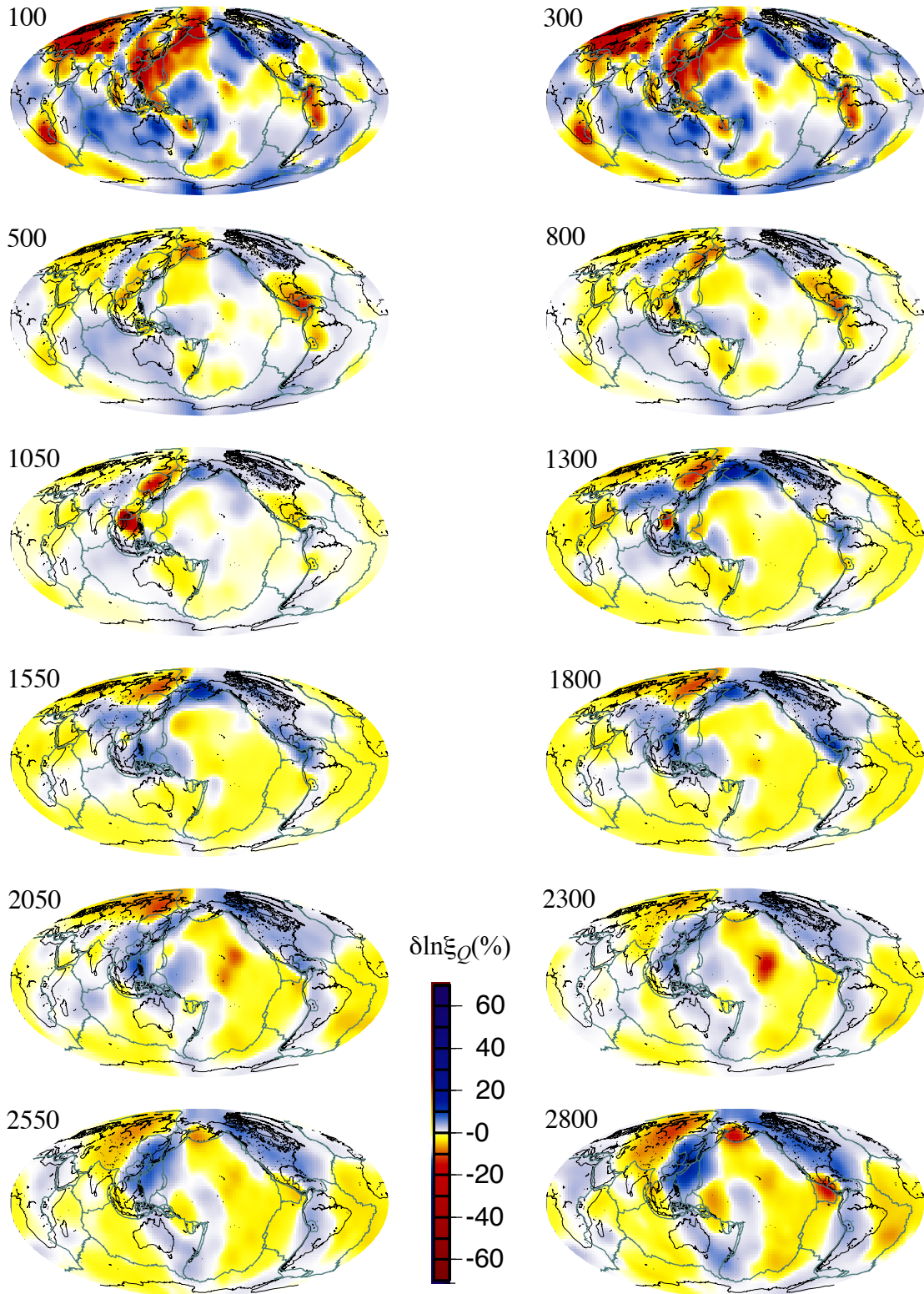
VQM3DA: Isotropic Quality Factor

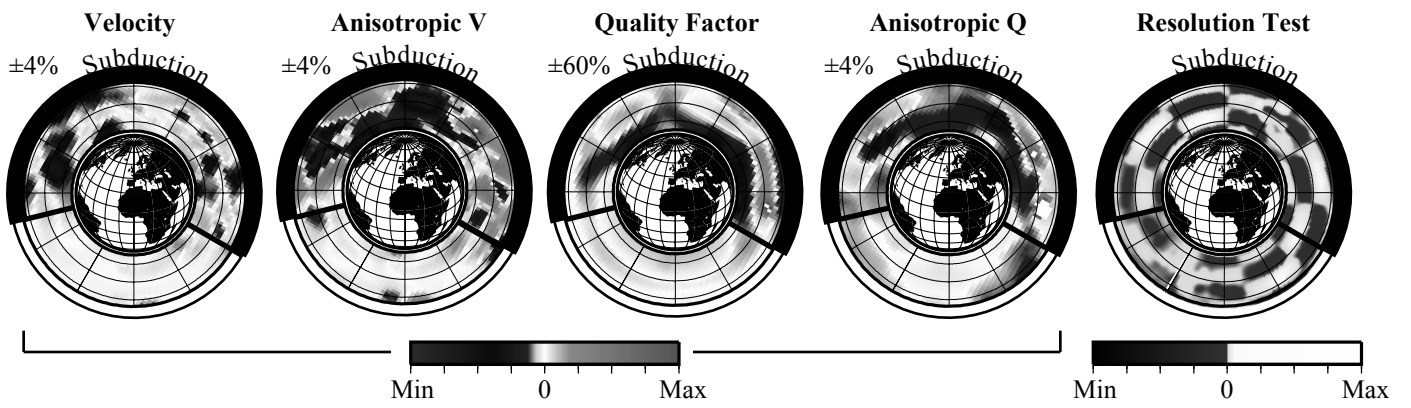


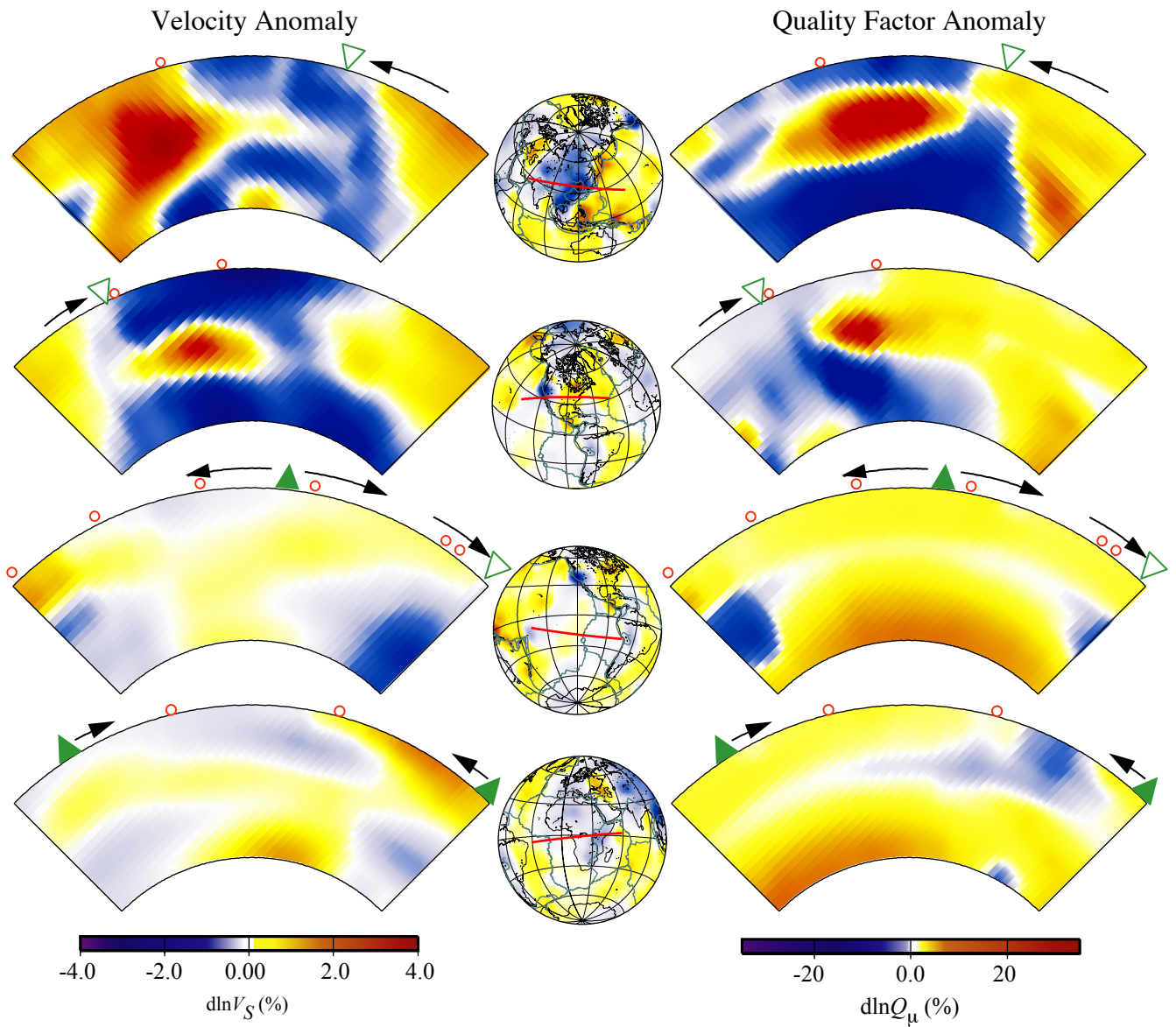
VQM3DA: Anisotropic Velocity

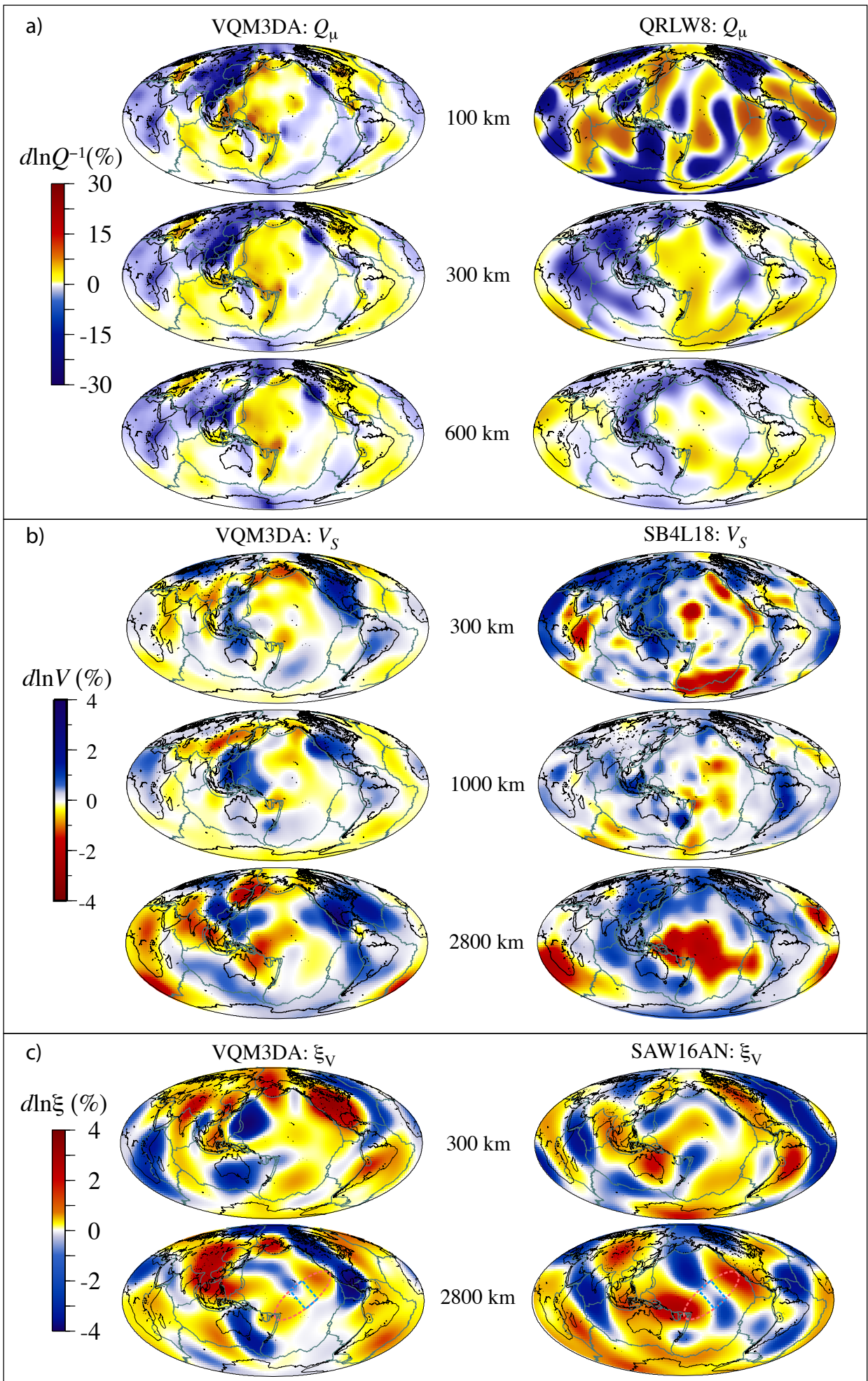


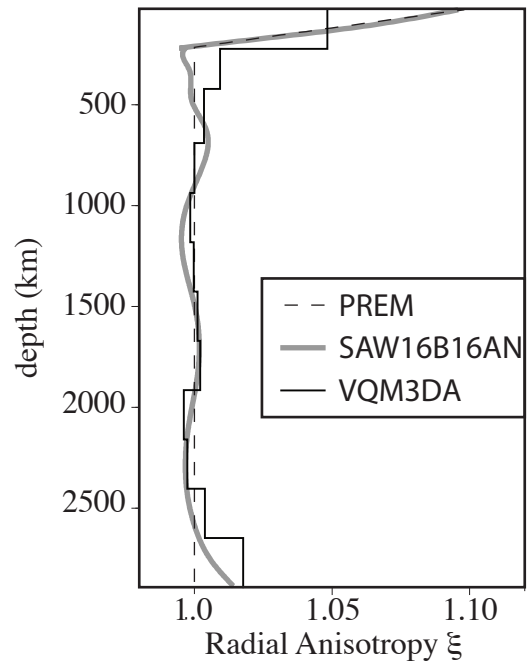
VQM3DA: Anisotropic Quality Factor

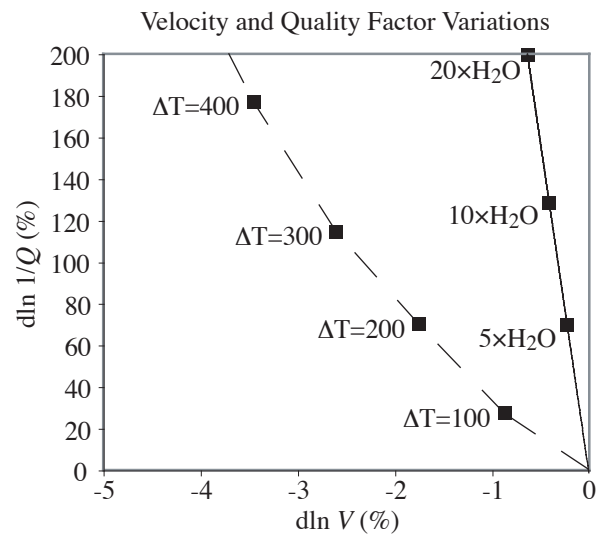












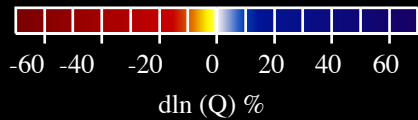
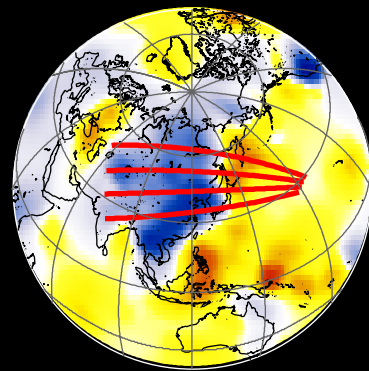
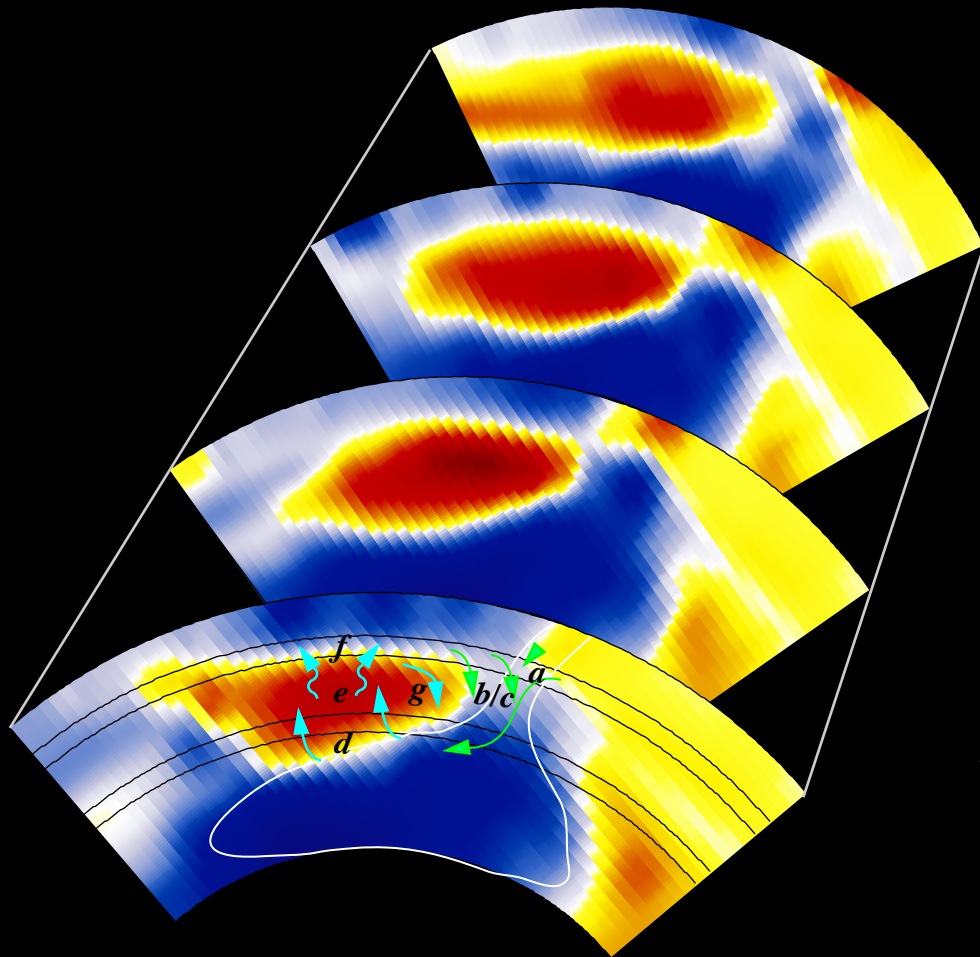


Figure 15

